Dual-REAdout Method experiment

Measurement of the Cherenkov light in a BGO crystal crossed by cosmic rays

Carnevale Rachele	**1950973**
Cipriani Arianna	**1898318**
Lupi Alessio	**1894162**
Pietropaoli Lorenzo	**1917791**

Under the supervision of
Fabio Cappella
Filippo Errico

Contents

Introduction

This report is going to give a thorough description of the DREAM experiment, which our group studied and attempted to reproduce in the past few months. As will be better explained in section 1, we want to measure the light yield from scintillation and Cherenkov effect in a bismuth germanate crystal traversed by vertical muons, as a function of the tilt angle of our apparatus. Our work mainly focused on: building and commissioning the experimental setup (section 2 and section 3), collecting and analyzing data with the aim of studying the ratio between the Cherenkov and scintillation light yields (section 4), and lastly implementing a `Geant4` simulation of the experiment, in order to validate the experimental results (section 5).

1 Theoretical outline

The DREAM (Dual-REAdout Method) experiment takes its name from a technique which aims at enhancing the resolution on calorimetric measurements. This improvement is achieved through the study of electromagnetic (EM) showers which, when interacting with the calorimeter, limit its resolution on hadronic jets. In particular, fluctuations of the EM showers can be substantially reduced by measuring separately the light yield from scintillation and Cherenkov light in the calorimeter.

Whilst it is a future goal to implement the DREAM method in the Future Circular Colliders, in our experiment we have tested its validity through a miniature version of a calorimeter, using a BGO (bismuth germanate) scintillating crystal interacting with cosmic muons as probes.

The ability to measure separately Cherenkov and scintillation contributions to the light yield in the crystal partly depends on the rather different nature of the two phenomena.

1.1 Cherenkov light

When a particle travels through a medium at a speed u greater than the speed of light in the medium, Cherenkov light is produced, forming a cone (Figure 1). The angle of emission (with respect to the direction of flight) φ_C is fixed by the particle velocity (β) and the refraction index (n) of the medium as follows:

$$\varphi_C = \arccos \frac{1}{\beta\, n} \qquad \text{with } \beta = \frac{u}{c} = \frac{p}{E} = \frac{p}{\sqrt{p^2 + m^2}} \tag{1}$$

which, in our case, gives $\varphi_C = 62°$. This value has been calculated assuming that the particle (a muon in our experiment) carries a momentum $p \approx 4\,\text{GeV}$ [1] and the BGO refraction index is $n = 2.15$. Knowing the rest mass of the muon to be $m_\mu \approx 105\,\text{MeV}$, the calculation is performed using the formulas in Equation 1.
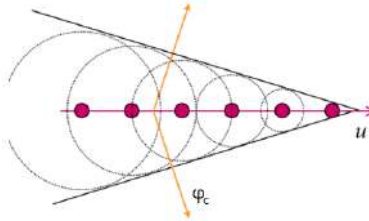
Figure 1 Scheme of Cherenkov light emission. The wavefronts of the emitted light lie on a cone with an aperture angle denoted as φ_C in the picture. [2]

2

Important features of Cherenkov light are its rapid emission and its polarization, with a spectrum that lies roughly in the UV range. Further on in this report, it will be discussed how these characteristics affect our analysis and allow us to distinguish Cherenkov light from scintillation light.

1.2   Scintillation light

Scintillation light is emitted isotropically in the visible spectrum when a charged particle ionizes the medium it is traversing, by excitation - and subsequent de-excitation - of the molecules of the medium itself. This process is generally slower compared to Cherenkov emission, depending on the scintillating material. This difference will be one of the most critical aspects in the separation of the two components of the light yield: in the BGO, indeed, one has a typical mean time of scintillation of few hundreds nanoseconds ($\approx 300\,\text{ns}$) and a typical time of the Cherenkov impulse of tens of nanoseconds ($\approx 20\,\text{ns}$).

1.3   Energy release

Energy loss by ionization in a medium follows the Bethe-Bloch formula

$$-\frac{1}{\rho}\left\langle \frac{dE}{dx} \right\rangle = C\,\frac{Z}{A}\frac{z^2}{\beta^2}\left[\ln\left(\frac{2m_e c^2 \gamma^2 \beta^2 W_{max}}{I^2} \right) - 2\beta^2 - \delta \right] \tag{2}$$

where $\left\langle \frac{dE}{dx} \right\rangle$ is the specific energy loss, and ρ the density of the material. The constant C is equal to $\frac{\pi e^4 N_A}{m_e}$, where e is the electron charge, N_A is Avogadro's number, and m_e is the electron mass. Furthermore, Z and A denote the atomic and the mass number of the material, respectively, z represents the charge of the incident particle. W_{max} corresponds to the maximum kinetic energy, I is the mean excitation energy and finally δ is the density correction. This is relevant to our experiment as it allows for calibration of the energy release distributions in both the BGO crystal and the trigger system, which also consists of scintillators[1]. In our case, since we are detecting cosmic muons with $\beta\gamma \approx 40$, we use the MIP (Minimum Ionizing Particle) approximation, which corresponds to an average energy loss of $2\,\text{MeV cm}^2/\text{g}$, as shown in Figure 2.
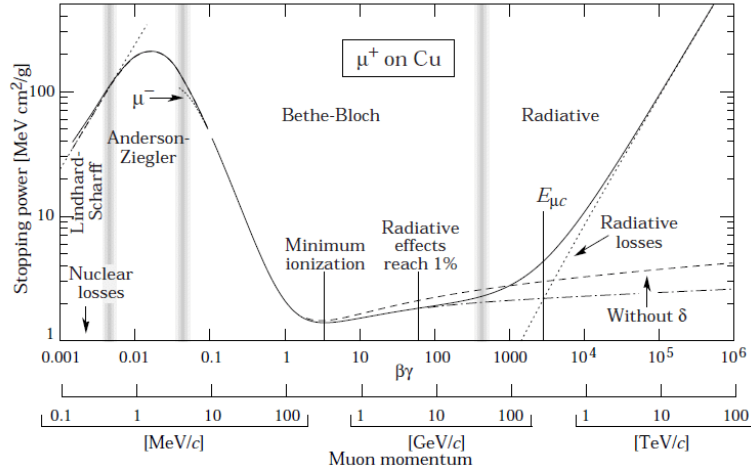
Figure 2 Total Bethe-Bloch energy loss of μ^+ in Cu. [3]

---

[1]A calibration procedure will be discussed in section 5, where we will cover the data simulation of our experiment. The trigger system will be explained in section 2, dedicated to the experimental setup.

Since the measure we carried out is independent of the calibration of the energy release in the detector, we postpone this part to section 5, in which calibration is taken care of for the simulation part of our study.

1.4 Angle dependence in our experiment

This is a good point at which to briefly introduce how the light yield (and hence the energy release) in our experiment depends on the angle at which our experimental apparatus is tilted. The apparatus will be covered in detail in section 2, so we will just mention that the BGO crystal is free to tilt at an angle with respect to the horizontal that we will name θ. This is a relevant choice in light of the fact that our apparatus selects the passage of vertical muons (note that in this way $\theta_C = \pi - \varphi_C = 28°$). The crystal is also instrumented with two PMTs, one devoted to Cherenkov and one to scintillation light detection. This makes in such a way that:

   a) the Cherenkov light yield in the crystal, due to the cone shape, will be an even function of the angle around a maximum, whose position we will look for;

   b) the scintillation light yield, being isotropic, will just vary as $\frac{const.}{\cos\theta}$, as the path that the muon covers when traversing the BGO:

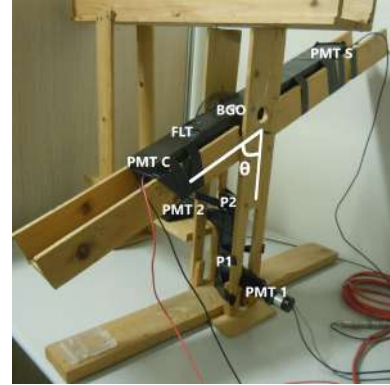$$\text{muon path} = \frac{d}{\cos\theta} \quad , \tag{3}$$

   with d the average thickness of the BGO.

2 Experimental setup

The experimental apparatus (which is visible in Figure 3) is centered around a 18 cm × 2.2 cm × 2.2 cm BGO crystal, which is encapsuled in a wooden structure that can tilt around a horizontal axis from $\theta = -45°$ to 45°. The crystal, along with two photomultiplier tubes (PMTs) coupled to its smaller faces, is positioned in a black box in order to minimize external light noise. The two PMTs are assigned to Cherenkov (PMT C) and scintillation (PMT S) light detection. Since scintillation light is produced in equal amounts in the direction of the two PMTs, a specific photomultiplier (with higher sensitivity in the UV range) has been used to detect the feeble Cherenkov signal, along with the additional coupling of a UV and a polarizing filter. The first blocks light in the visible spectrum, in which a part of the scintillation spectrum lies. The second filter instead allows for only polarized light to go through it, which is also crucial since Cherenkov light is polarized.

Figure 3 A side view of the detector, with labels according to Table 1.

Just below the black box are two 1 cm × 5.5 cm × 9.5 cm trigger scintillators (P1 and P2), each coupled to a PMT (PMT 1 and PMT 2). They are held together vertically, with their smallest faces in contact, in order to only accept approximately vertical muons.

When a vertical muon traverses P1 and P2, the signals produced in the PMTs activate the trigger system, which is managed by the electronics crate (EC, Figure 4). The EC performs several other functions, including high voltage supply to the PMTs and more that we will discuss in the following section.

If the trigger system detects a potential event, signals coming from PMTs 1, 2, S and C are sent to the transient digitizer (TD, Figure 4), which allows for data acquisition and storage in the computer, as will be explained in subsection 2.2.

The PMTs have been supplied with voltages $V_{\text{PMT 1}} = (700\pm1)\,\text{V}$, $V_{\text{PMT 2}} = (1800\pm1)\,\text{V}$, $V_{\text{PMT C}} = (940\pm1)\,\text{V}$, $V_{\text{PMT S}} = (993 \pm 1)\,\text{V}^2$.

Table 1 breaks down the various components of our setup.

Table 1 A brief description of the main features of the components of our detector (P1, P2 to FLT), as well as the electronics logic units (A to F) and device for data transfer to the computer (TD and BRG).

Symbol	Name	Description
P1, P2	Plastic scintillators	Fast scintillators for trigger.
PMT 1, 2	Photomultiplier tubes	Relative to P1 and P2.
BGO	BGO crystal	Detector. From the passage of muons may occur scintillation and Cherenkov light emission.
PMT C	Photomultiplier tube	Dedicated to Cherenkov light.
PMT S	Photomultiplier tube	Dedicated to scintillation light.
FLT	Filters	A UV and a polarizing filter for Cherenkov light detection enhancement.
A	CAEN N471	HV power supply modules.
B	CAEN N401	Fan-in fan-out (FIFO). It is used for signal duplication.
C	CAEN N96	Discriminator. It converts analog signal to a 800 mV square wave with adjustable width, if the signal exceeds a threshold. Time width and threshold are given as inputs from the user.
D	LeCroy 465	Coincidence unit, used to establish coincidence between the PMT 1 and 2 signals.
E	CAEN N145	Scaler and counter. It can be used as a counting device in two ways: either given a stopping time or a maximum count value.
F	CAEN N108	Dual delay. It can be used to add up to $63\,\text{ns}$ time delay to a signal.
TD	CAEN V1731	Transient digitizer. It converts analog into 8-bit digital signals. It has been used in 1000 megasamples/s mode (= 1 sample per ns), which requires using only 4 out of the 8 available channels. It's saturated by signals greater than $1\,\text{V}$.
BRG	CAEN V1718	Bridge. It connects the TD to a computer used for data analysis.

---

^{2}The significantly different HV supply for the two plastic scintillator is motivated in section 3.
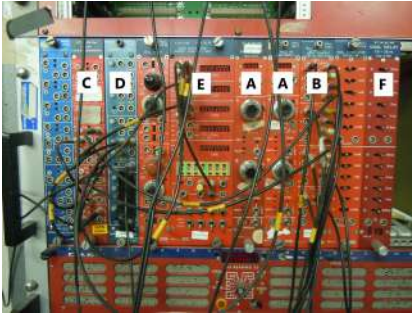
(a) Electronics logic units (A to F).
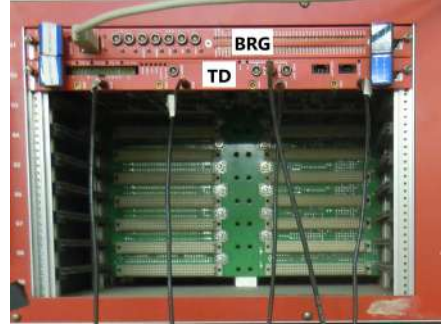
(b) Transient digitizer (TD) and bridge (BRG).

Figure 4 Pictures of the electronics crate.

2.1 Trigger system

The trigger system allows the detection of an event if both PMTs 1 and 2 send a signal to the discriminator module with an amplitude greater than a threshold value, and within a time window of $\approx 30\,$ns (or less) relative to each other.

Here is an overview of how it operates:

1. The main hardware part of the trigger is constituted by the two plastic scintillators, P1 and P2, and their respective photomultipliers, PMT 1 and PMT 2. These convert the scintillation light into an electric signal. Since P1 and P2 are intended to detect the passage of vertical muons, they are placed so their geometrical acceptance greatly favors such events, as visible in the picture in Figure 3.

2. When P1 or P2 scintillates, the corresponding signal from PMT 1 or PMT 2 is sent into a channel of the fan-in fan-out (FIFO) unit (B). The FIFO creates a number of copies of each signal that is fed into one of its channels. The FIFO duplicates both signal coming from the two photomultiplier tubes: one copy is directed to the transient digitizer (TD), which via the bridge unit (BRG) directly sends it to the computer for data analysis, while the other is properly used for trigger.

3. The signals are then processed by the discriminator module (C): as soon as they exceed a user-set threshold value, the discriminator produces a square wave of adjustable time width. In this case, one copy of both signal coming from the fan-in fan-out goes to the discriminator, which produces a 400 ns square wave for each signal if they exceed a voltage threshould set around 60 mV (a more detailed analysis on the voltage threshold is provided in section 3). Choosing both an appropriate threshold value and a time window of 400 ns for the square signal guarantees that no late ripples[3] in the scintillation signals activate the discriminator and get interpreted as passage of a second muon in the detector.

4. While the third step is an intermediate phase in the generation of a logic signal that represents the *time window in which a vertical muon is traversing the detector*, the fourth step finalizes that process. The signals originally coming from PMTs 1 and 2 are fed, after the initial discrimination, into two other channels of the discriminator unit, which is now set up to only shrink the time duration of the square wave from 400 ns to 30 ns. This is a value that should be chosen of the order of the typical scintillation time of the plastics P1 and P2, so to faithfully reproduce the time window of the true passage of a muon. This is of course aimed at the following step, which establishes the coincidence between the signals from the two scintillators. The typical scintillation time of the plastics is about 5 ns, so 30 ns feels like an appropriate choice.

---

[3]Late ripples could occur, for example, as the signal stabilizes after having reached its peak.

5. The final step consists in determining whether two signals from PMTs 1 and 2 correspond to the same vertical muon passing through the detector. This is achieved by the coincidence unit (D), into which the signals from PMTs 1 and 2 are fed after the whole elaboration process described in the previous steps. The logic unit essentially checks for overlap between the 30 ns-square waves, as that would represent a true coincidence. If an overlap is detected, a logic output is sent from the coincidence unit to the transient digitizer, it works as clock start for the acquisition of the four analog signals coming from PMTs 1, 2, C and S. This will be seen more in-depth in the following section.

6. (optional) Additional analysis may involve also the delay unit (F) of the electronics crate. By introducing a time delay to the signal received as input, this unit typically helps in studying accidental coincidences that statistically occur in the trigger. This will be explained in section 3.

2.2 Data acquisition

When the trigger system detects the passage of a vertical muon, the signals from PMTs 1, 2, C and S are analyzed, with the primary goal being the measure of the ratio of Cherenkov to scintillation light.

The signals from the PMTs are sent to the transient digitizer (TD): the PMT C and PMT S signals go directly, while those from the PMT 1 and PMT 2 are duplicated also for the trigger building procedure, as explained earlier. The TD effectively does an analog-to-digital conversion of the signals, which are then transferred to the computer for analysis via the bridge module (BRG).

This procedure begins with the triggering event, but the signals are actually recorded starting from 100 ns before the trigger. This has been set up in order to enable baseline analysis, which involves studying the default value associated to a 0 V signal in the data acquisition (DAQ) system. The acquisition time for each signal is 960 ns, including baseline information. This guarantees that even the longer, BGO scintillation signal (which typically lasts hundreds of ns) is fully recorded by the DAQ system. It's crucial to not lose any information that regards the signals, especially for the calculation of some physical quantities like the energy release in the crystal, which is proportional to the area under the signal curve.

The digital conversion by the TD is managed by a `C++` DAQ program, which allows the user to set various parameters before each data acquisition run. For example, one can specify the total acquisition time, during which many events occur, hence a large number of signals are recorded and stored to disk in the computer in a `ROOT` file. In our experiment, each run acquisition time was about three days to collect sufficient data. It is known that approximately one muon hits every square centimeter of the Earth's surface every minute at sea level, but this rate would be an overestimate in our experiment since we detect only vertical muons.

A separate `ROOT` file is created for each data acquisition run. This file is then read through another `C++` program, in order to do data analysis. In section 4 we will explain how we analyze the signals in light of the observables we want to reconstruct. Before that, a section regarding the commissioning of the detector is going to follow.

3 Commissioning

This section will explore the commissioning phase, a preparatory stage that needs to come before the proper data taking and analysis. During this phase, the working parameteres of the detector are studied and characterized.

The first part will cover the study of the voltage threshold that needs to be imposed on the discriminator unit (see subsection 2.1) to differentiate between signal associated with the passage of muons and that which is not. Then a study on accidental coincidences between the two trigger scintillators will follow, in order to estimate and predict the effect of unphysical coincidences that occur statistically in the trigger system on our analysis. A brief part motivating and explaining the usage of a Cherenkov polarization filter will follow. Then, the time jitter effect will be explained, including its effects on the distribution of the times of start of the PMT signals,

as well as a solution to mitigate this effect (which, in principle, represents an obstacle). Lastly, a paragraph on signal saturation will close the commissioning section.

3.1 Noise evaluation and study of the voltage threshold

We need to determine whether the plastic scintillators P1 and P2, that make up the trigger, detect the actual passage of muons or merely noise. A noise component is indeed going to be present independently of the signal associated to the muons, and we wish to establish a threshold voltage value for the discriminator unit (see section 2 for more detail), above which to interpret the signal as a true event and under which to ignore it.

To achieve this, we performed count measurements in both the plastic scintillators, over $\Delta t = 300\,\text{s}$, while varying the threshold voltages V_{th_1} and V_{th_2} to determine the appropriate threshold required for event detection. The choice of this time interval stems naturally from muon rate considerations ($R_\mu = 1\,\text{cm}^{-2} \cdot \text{min}^{-1}$) and assures that enough statistics is available to make the signal emerge over the noise background. The counting procedure, including the acquisition time, was for this phase managed by the scaler/counter unit (E). The threshold voltages are adjusted using the discrimimator module (C), within the range $[-255, -35]\,\text{mV}$.

The expected behavior is an exponential decrease. This can be understood as follows: the noise should correspond to a roughly constant value but manifests as a rapidly oscillating signal that repeatedly triggers the detector unless the threshold is set at a high enough voltage. For relatively high threshold values (above $100\,\text{mV}$), the recorded counts should correspond most of the times to true signal rather than noise fluctuations. The in-between is a smooth transition from the region dominated by noise (resulting in a high number of counts) to a plateau-like region that corresponds to true signals. In this transitioning region is to be found the knee-point which should represent a shift from the first to the second behavior. Figure 5 shows the experimental results of this analysis.
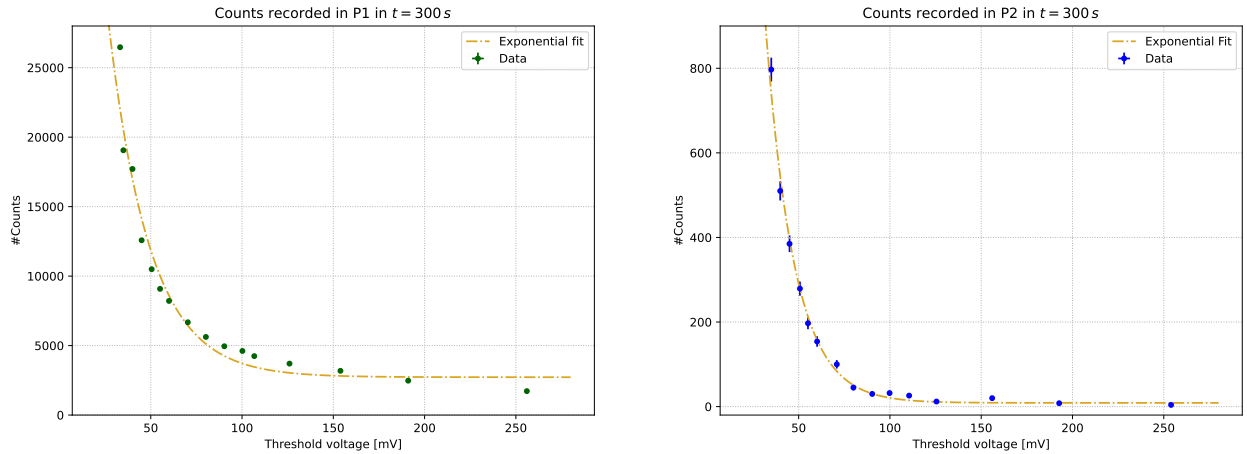

Figure 5 Exponential fit on the data recorded in the two scintillators over $300\,\text{s}$. Counts with Poissonian errors are represented as points, while a single-exponential fit to the points is also reported for show. Both plots exhibit a decreasing exponential trend due to the reduction of noise sensitivity as the voltage threshold rises. There is also a difference in the orders of magnitude of the counts in the two channels, highlighting a different noise level (hence different amplification) of the two PMTs, though this does not affect our analysis.

As one can see, the experimental points distribute along the convolution of two exponential curves. The steeper, leftmost behavior can be attributed to noise, while the one on the right is dominated by signal, especially as it approaches the region in which the points lay on a plateau. This is consistent with the expected behavior. It is worth noting that PMT 1, which was replaced by us this year, exhibits a larger amplification constant with respect to PMT 2, which is related to a higher noise level of the photomultiplier, as can be seen in the

experimental plots. This discrepance, though, does not affect the search of the threshold, in that both noise and real signal get amplificated equally, and this effect does not modify the value of the working voltage point we look for as it only affects the amplitude of the expected behavior.

With the aim of identifying the best threshold voltages to set for the two channels (something that needs to be found as a working point to be kept fixed throughout the experiment), we performed a linear fit on the experimental data. The working point was identified as the knee-point between the different behaviors aforementioned. Different fitting techniques were employed for the two channels: for P1 we fitted linearly the logarithm of the data, while for P2 we performed linear fits directly on the distribution of counts. Figure 6 shows the fitted behaviors.
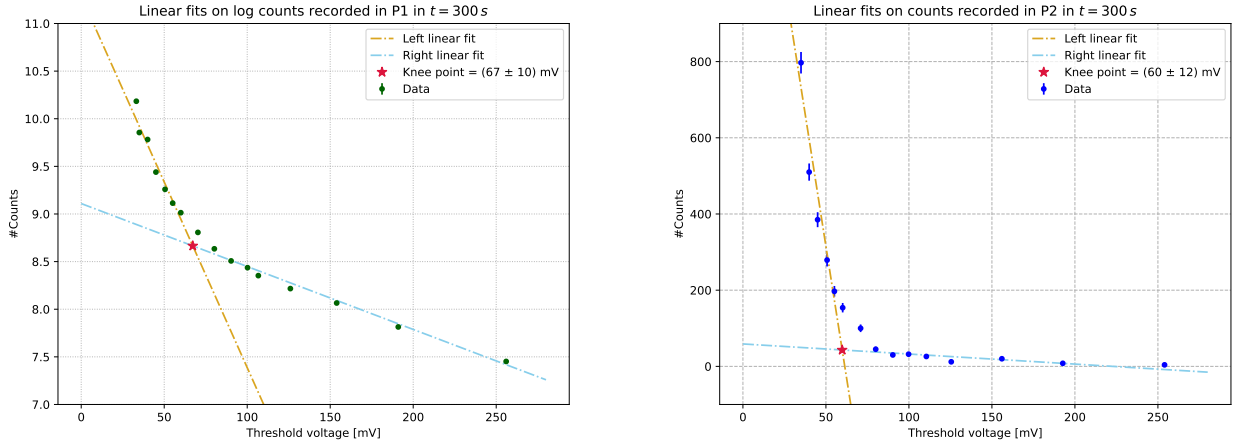
Figure 6 (Left) Double linear fit on the logarithm of counts in the P1 channel. (Right) Double linear fit performed directly on experimental points (counts) in the P2 channel. This double-behavior fit is useful in order to identify a knee-point where the high-count trend, due to mostly noise, joins the flatter, stable region in which counts are actually due to vertical muons that trigger our detector.

The points once again correspond to the recorded counts, while the dashed curves are those that best fit the data in the two regions. The way we defined the regions (noise-dominated and signal-dominated) was based on mere observation of the experimental data: they correspond to the intervals [first 8 points/last 7 points] (noise/signal) for channel P1 and [first 8 points/last 8 points] (noise/signal) for channel P2.

The results from the fit, including statistical uncertainty, suggest the following results:

$$V_1^{th} = (67 \pm 10)\,\text{mV} \qquad\qquad V_2^{th} = (60 \pm 12)\,\text{mV} \quad . \tag{4}$$

These values were fixed on the discriminator unit setup panel permanently after this stage of the commissioning analysis. All counts and results that appear in the following sections rely quite heavily on the choice of these thresholds.

3.2 Study of accidental coincidences

In the process of limiting false events by tuning the setup of the detector, it is necessary to study the effect of those false events that cannot be completely eliminated due to various factors. These are referred to as accidental coincidences, that essentially happen when two signals trigger the detector but do not come from the same muon event. Just as an example, in a rather improbable (but still possible) case, a false coincidence could arise from two muons hitting P1 and P2 within a short-enough time window (in our case, $\tau_1 = 31.4 \pm 4.0\,\text{ns}$ for PMT 1 and $\tau_2 = 32.6 \pm 4.0\,\text{ns}$ for PMT 2). The most likely cause, though, is the cross-talk between the

induced signals by the two photomultipliers in the electronic chain.

Nothing can be done, in our experiment, to completely prevent accidental coincidences. Of crucial importance is, of course, the physical setup of P1 and P2 (which one can be reminded of in section 2), whose geometrical acceptance cuts out already a substantial part of potential false coincidences. In this paragraph we wish to quantify the extent of the remnant part of this phenomenon: accidental coincidences cannot be entirely eliminated, but if their occurrence rate is found to be negligible, then one can proceed the analysis without worrying that the results will be affected by a small fraction of false events. It is also probable that further analysis will show these false events lying far from the bulk of the distributions we are interested in.

The rate of accidental coincidences registered in a two-level trigger like ours can be predicted, assuming a Poisson distribution for the counting process and given the expected rate of counts of the two scintillators, using

$$R_{th} = R_1 \left(1 - e^{-R_2\tau}\right) + R_2 \left(1 - e^{-R_2\tau}\right) \approx 2R_1 R_2 \, \tau \tag{5}$$

where R_1 and R_2 are the rates of counts from scintillators P1 and P2, and τ is the time window of each trigger scintillator (we can assign a unique value to the two time windows). The observed rate of coincidences can be calculated from $R_{obs} = N_C/\Delta T$, where N_C is the number of random coincidences and $\Delta T = 10^4$ s the total run time (chosen in such a way that we could get sizeable statistics). We recorded

a) the rate of counts for the P1 channel

b) the rate of counts for the P2 channel

c) the rate of observed coincidences between the P1 and P2 channels using the coincidence unit.

This was done for four different configurations of the two plastics:

1. The two scintillators placed one above the other, with their larger surfaces in contact: we expect the largest number of observed coincidences in this configuration, as it is the one that maximizes the geometrical acceptance for the trigger;

2. The two scintillators one above the other, with their smaller surfaces in contact: the configuration intended to be used in the experiment, as it best restricts the acceptance to include only vertical muons;

3. Scintillators set apart by approximately one meter, in no precise relative orientation: this configuration geometrically disfavors false coincidences;

4. Scintillators set apart by approximately one meter with an additional 63 ns time delay (implemented using the dedicated logic unit): this setup is even less favorable for coincidences.

The aim of the analysis is to compare the expected versus the theoretical coincidence rates. In the last two configurations we expect only accidental coincidences, so the observed rate should agree with the predicted one. On the other hand, we do expect also "physical" coincidences in the first two configurations, so the rate should be higher in those cases.

We conducted one acquisition run for each configuration, counting events in both scintillators (N_1 and N_2), and observed coincidences (N_{obs}), with the uncertainty equal to $\sigma_N = \sqrt{N}$ (Poissonian). We evaluated the rate by $R = N/\Delta T$, with $\sigma_R = \sigma_N/\Delta T$, assuming negligible uncertainty on time setting.

Table 2 presents our results.

Table 2 Measured rates of counts in the two plastic scintillators (R_1 and R_2), observed rate of coincidences R_{obs} measured with scaler and theoretical expected rate for accidental coincidences R_{th}.

Configuration	R_1 [Hz]	R_2 [Hz]	R_{obs} [Hz]	R_{th} [Hz]
1	21.734 ± 0.047	0.3175 ± 0.0056	0.2014 ± 0.0045	$(4.42 \pm 0.40) \times 10^{-7}$
2	24.392 ± 0.049	0.4803 ± 0.0069	0.0301 ± 0.0017	$(7.50 \pm 0.67) \times 10^{-7}$
3	20.586 ± 0.045	1.128 ± 0.011	$< 2.3 \times 10^{-4}$	$(1.49 \pm 0.13) \times 10^{-6}$
4	13.299 ± 0.036	1.025 ± 0.010	$< 2.3 \times 10^{-4}$	$(8.72 \pm 0.78) \times 10^{-7}$

The rate of observed coincidences R_{obs} lies, as expected, above the theoretical expectation value R_{th} for the first two configurations, where also physical coincidences are expected, while on the other hand it's compatible with R_{th} for the last two configurations. In particular, to the registered rate of $0\,\mathrm{Hz}$ for the last two configurations, a Poissonian upper limit of $2.3 \cdot 10^{-4}$ was assigned.

3.3   Polarization of Cherenkov light

The typical light yield of scintillation light in a crystal is orders of magnitude larger than the typical Cherenkov light yield in the same material. This implies that

  a) when it comes to detecting scintillation light, little to no contamination from Cherenkov effect need be considered;

  b) instead, when measuring the Cherenkov light yield in the BGO, one needs to account for strong contamination from scintillation light.

As we already cleared up, Cherenkov light is emitted - and hence needs to be detected - at an angle. Furthermore, it is polarized, unlike scintillation light. This has a significant impact on the ability to reduce contamination from scintillation light to the Cherenkov yield: as was the case in our experiment, good isolation of the Cherenkov light yield was obtained by a combination of polarizing and UV series of filters interposed between the BGO and PMT C.

A brief characterization phase was needed for the polarizing filter, since we received no information on its usage specifications. The filter had a little lever that could be set in two positions, which we labeled "left" (L) and "right" (R)[4]. We proceeded to test those two settings by collecting data with both positions of the filter. We remind the reader that Cherenkov light detection in our experiment is heavily dependent on the tilt angle of our apparatus (see again section 2), so data was taken around the angle of maximum expected Cherenkov light yield, approximately 28°. In practice, angles of 28° and 30° were investigated, both providing evidence for the "R" position to be the Cherenkov-favoring one. This position of the filter would be the one to keep for the rest of our experiment.

Figure 7 shows the results of our analysis.

---

[4]With no actual reference to *left* or *right* polarization, but rather to the physical position of the lever.
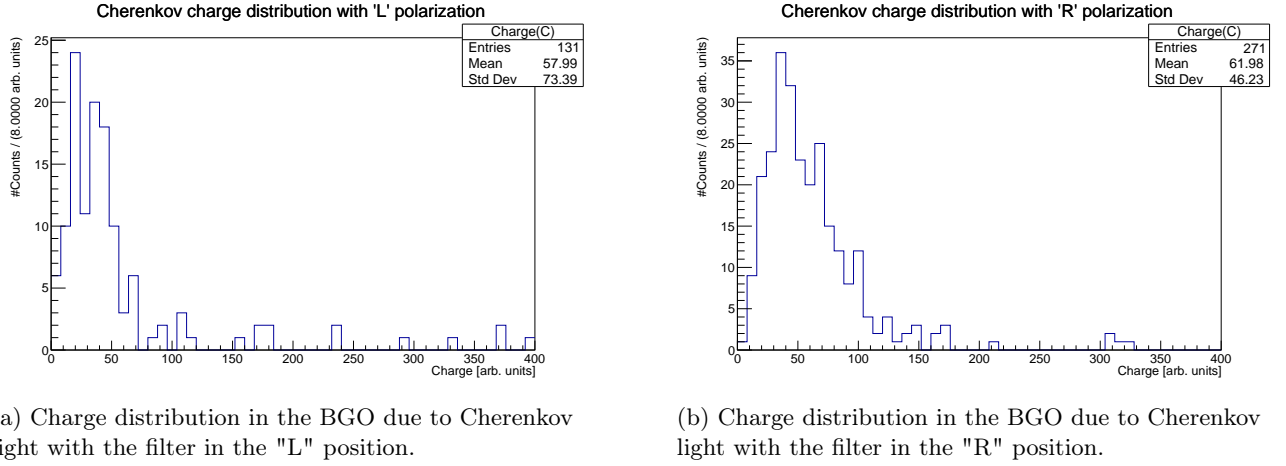
(a) Charge distribution in the BGO due to Cherenkov light with the filter in the "L" position.

(b) Charge distribution in the BGO due to Cherenkov light with the filter in the "R" position.

Figure 7 Energy release due to Cherenkov in the BGO crystal in the two different positions of the UV filter at θ=30.8°.

The two plots show the charge (i.e. the integral of the signal) in arbitrary units released in PMT C as an event-by-event histogram, in the two orientations "L" and "R" of the polarizing filter coupled to PMT C, for a crystal tilt angle of 30.8°. We will refer to this angle as θ^*, as will be useful also in section 5. This angle was chosen since it is in the region of maximum Cherenkov light production. One can clearly see, over the exponential background of other sources of electric signal in the PMT, a bump that is present around 100 (arbitrary units of charge) in the case of the "R" position and not in the case of the "L" position.

As will be seen in a more detailed analysis of the light yield, a quantity proportional to the energy released in the crystal and in the PMTs, the expected signal appears as a peak against an exponential background. The latter is associated with non-vertical muons. A large number of events usually corresponds to either non-vertical muons or noise fluctuations that still produce a signal in our detector, but the corresponding value of the signal charge (and also for other observables) statistically distributes over a broad interval. In the case of charge, this distribution is exponentially decreasing.

The presence or absence of this peak then suffices to establish that the correct position of the polarizing filter to adopt for the rest of the experiment is the one for which the bump of counts is present in the distribution, which is the "R" position.
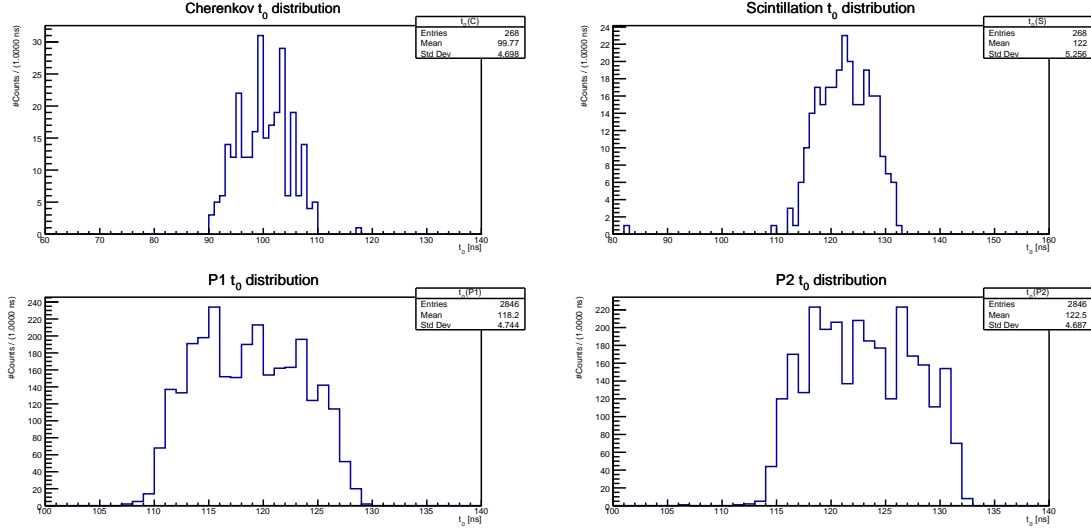
3.4   Time jitter correction

Another observable to examine during the commisioning phase is the distribution of the time of start of the signals from the four channels (P1, P2, C and S). The reason for this is that it is known that the transient digitizer introduces a random and uniformly distributed time offset to each recorded time value associated with a sample of an electric signal. This jitter is distributed in the interval [-16, 16] ns.

To achieve more precision in our analysis, one could mitigate this effect by means of a rather simple technique. Since the events we are interested in are triggered, the time of passage of a vertical muon in our trigger system represents a possible, natural choice of clock reference for time value recordings associated to signal samples. In other words, we choose to count time not starting from the clock time given by the digitizer, which suffers from the jitter effect, but rather from the trigger time, which can be easily determined as the mean value of the time of start t_0 of the signal in P1 and P2 (the trigger scintillators) for each event:

$$t_{\text{clock}} = \frac{t_0(\text{P1}) + t_0(\text{P2})}{2} \quad . \tag{6}$$

12

Looking at the time of start of the signals, one can notice the jitter effect broadening the distributions before the clock start correction (Figure 8) and compare this with the same distributions after the correction of this effect (Figure 9). Naturally, having shifted the clock start to the time of trigger, all time of starts now distribute around 0 ns, with a much narrower width and a roughly Gaussian shape, unlike the distributions before the jitter correction. These last are still vaguely centered around the correct time of trigger value, but with a rather flat shape which is typical of a uniform distribution.

Figure 8 Distributions of the time of start of the signal for Cherenkov, scintillation, P1 and P2 channels before jitter correction. One can observe a flat, uniform-like distribution centered around a value of roughly 100 ns, which corresponds to the time of start of the event. On this note, it is useful to remember that the actual time recorded by the DAQ system begins about 100 ns before the actual start of an event, allowing for signal baseline reconstruction.
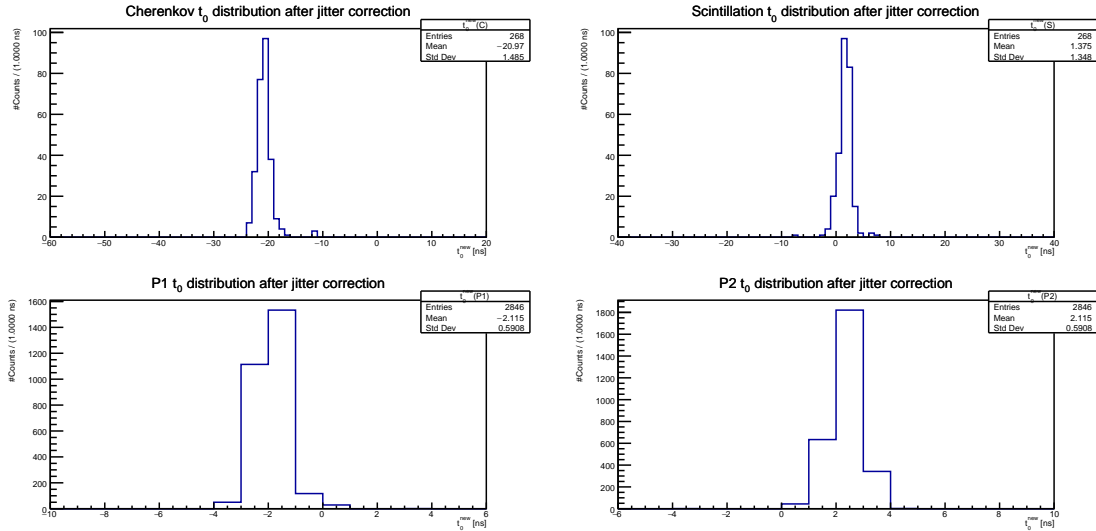
Figure 9 Distributions of the time of start of the signal for Cherenkov, scintillation, P1 and P2 channels after jitter correction. The once flat distributions are now much narrower and closer to a Gaussian in shape, suggesting a betterment in the time resolution capability. The start times are now centered around 0 ns, as a consequence of the fact that they are calculated with respect to the true time of passage of the muon in the trigger system. The ≈ 20 ns shift in the Cherenkov channel is likely due to the differences in the response times of the PMTs, leading to Cherenkov signal initial times being centered around a slightly negative value.

In particular, the new signal start times are obtained from the old ones using the formula
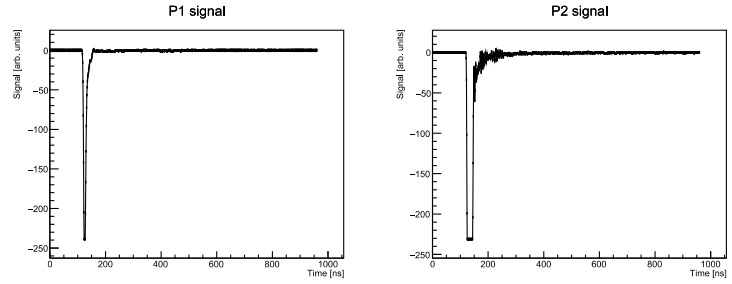
$$t_0^{\text{new}}(\text{Ch}) = t_0(\text{Ch}) - \frac{t_0(\text{P1}) + t_0(\text{P2})}{2} \quad , \tag{7}$$

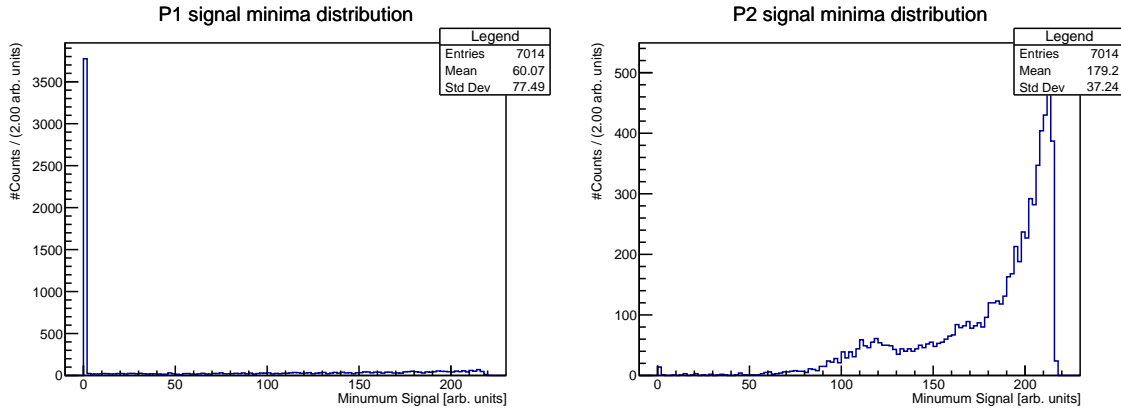with Ch = {C, S, P1, P2} the four channels and $t_0(\text{Ch})$ their relative signal start time for an event.

3.5 Study of signal saturation

Upon examining the first data runs we took, it was quickly realized that some saturation of the digitizer had occurred. While Figure 10 shows the saturation of a single event, Figure 11 contains event-by-event distributions of the signal minima recorded by the digitizer. The minima distribution was chosen as a good observable to look at for discerning and studying this saturation effect, as the minima distribution highlights a most frequent value that is clearly not physical, being the minimum value that the 8-bit digitizer can handle (0 mV).

Figure 10 A saturated event seen on the channels P1 and P2. Whilst the saturation effect in our experiment mainly occurs in channel P1, this particular event shows saturation on both trigger channels, with the P2 channel having an even more evident saturation.

The solution to this problem was straightforward. By lowering the voltage supply to the PMT showing this effect (and that is the one with larger amplification), it was observed that the percentage of saturated events (the number of saturated events over the total number of events) decreased substantially and even approached zero, with a HV value that still guaranteed sufficient amplification power to the PMT without suppressing excessively the signals. Overall, the high voltage supply was lowered from 1000 V to 700 V only for the PMT that showed saturation (PMT 1, coupled to scintillator P1), which was enough to make the issue practically disappear, as can be seen in the Figure 12.

Figure 11 (Left) Histogram of event-by-event signal minima distribution at 28° tilt angle, for $V_{\text{PMT 1}} = 1000$ V. A high percentage of saturated event is clearly filling the 0 V bin. (Right) Histogram of event-by-event signal minima distribution at 28° tilt angle, for $V_{\text{PMT 2}} = 1000$ V. Little to no saturation is shown.
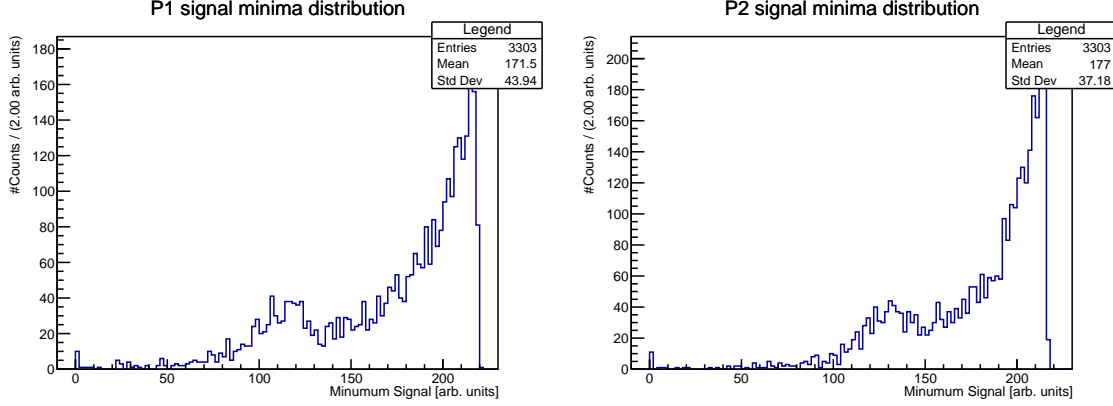
Figure 12 (Left) Histogram of event-by-event signal minima distribution at 28° tilt angle, for $V_{\text{PMT 1}} = 700\,\text{V}$. Little to no saturation is shown as a consequence of having lowered the HV supply to PMT 1. (Right) Histogram of event-by-event signal minima distribution at 28° tilt angle, for $V_{\text{PMT 2}} = 700\,\text{V}$. Little to no saturation is shown.

4 Data analysis

After the commissioning of the detector and the study of various unwanted behaviors for which we were generally able to find a solution (e.g. analysis of false coincidences, time jitter effect and signal saturation), the data acquisition chain was ready to be put into operation.

With the DAQ system working as described in subsection 2.2, we remind that for each acquisition run we took data for roughly 72 hours. In this time window we typically collected a total number of candidate events (events that trigger our detector, so in principle vertical muons) ranging between 1500 and 3000. The actual number could be seen slowly decreasing throughout the duration of the data taking (May to July 2024). This reduction may be attributed to either a deterioration of the trigger PMTs' internal amplification or the optical coupling of the PMTs to the plastics getting worse over time. As previously mentioned, this year our DREAM group replaced PMT 1 because of suspected amplification issues, which were also reported by last year colleagues in their report.

Hereafter, we will describe a series of cuts that were performed on the whole sample of events in order to identify the signal coming from vertical muons. This relies highly, but not exclusively, on analyzing the energy release in the BGO in the form of Cherenkov and scintillation light.

Lastly, we will present the results of the analysis, which is mainly targeted at the determination of the Cherenkov to scintillation (C/S) light yield ratio (a pure number) versus the angle of inclination of the BGO crystal (see again section 2).

4.1 Event selection

The process of event selection required some preparation. First of all we characterized, in each of the four channels (P1, P2, S and C), the **baseline** of each signal, i.e. the "zero" value of each channel, which is in principle constant and pre-set in the DAQ computer program. Together with the baseline, the **time of start** of each signal (which was used in the commissioning phase as well, as seen in subsection 3.4) was also calculated as follows:

1. Baseline voltage: the mean value of the first 80 samples (corresponding to the first 80 ns of acquisition) of

each signal. We associated also a standard deviation to the baseline voltage, which comes in as a critical factor in determining the start time of the signal;

2. <u>Time of signal start</u>: the time instant where the signal departs from the baseline by more than three times the baseline standard deviation for three consecutive sample points. Naturally, this start time value was then corrected to account for the jitter effect, as explained in subsection 3.4: this "new" t_0 (which loses the physical information on when the signal actually starts) was dubbed t_0^{new}.

Some other critical observables were analyzed in deciding upon which cuts to perform:

3. <u>Charge</u>: the time integral of the signal, performed from t_0 to a "safe" endpoint where the signal is expected to have returned to the baseline. The chosen integration intervals were $[t_0, t_0 + 50\,\text{ns}]$ for the fast scintillation channels P1, P2, and for the Cherenkov channel, and $[t_0, t_{\text{sample}}]$ (with $t_{\text{sample}} = 960\,\text{ns}$ being the total sampling time for each event) for the BGO scintillation channel. The 50 ns interval was chosen to fully include fast signals while being short enough to avoid late ripples that could distort the computation. The slower scintillation signal was instead integrated on a much wider interval, ending at the last sample time. This choice is of course motivated by the much more gentle slope of the signal, that often ends a few tens of nanoseconds before the sampling end time. Ripples after the signal were considered negligible, contributing minimally to the signal;

4. <u>Mean time</u>: the mean value T_{mean} of the time associated to a signal, i.e. the weighted average of the time samples, with the signal itself as weight.

5. <u>Signal minimum</u>: the minimum value reached by the signal (negative in our DAQ system). This was particularly useful in the commissioning part, as subsection 3.5 reminds.

All these quantities were computed upon reading each `ROOT` data file (each corresponding to a different tilt angle of the BGO) using a `C++` data analysis program, through which we implemented the following cuts. These were applied to each data file, and hence the analysis technique is independent of the BGO angle:

i) **first cut: t_0 presence**: a first discrimination was made by ruling out all the events in which *on at least one of the three channels* (P1, P2, S) no signal was detected. The Cherenkov channel was excluded from this condition on t_0 to avoid excessively reducing the signal detection efficiency, given that the Cherenkov signal is less intense, thus the most difficult to distinguish from noise and background.

This cut eliminated roughly 85% of the original events. Practically all the events that do not survive this cut present a signal in PMT 1 and PMT 2 (the trigger channels), but not in PMT S. Due to the geometrical structure of our detector, this appears as a quite likely occurrence, since the two trigger plastics P1 and P2 are rather close together, compared to their distance from the BGO. In practice, this cut was performed on the value of t_0 that was assigned to each signal for each event: if no significant (3 std. dev.) detachment from the baseline of the signal was detected (see above description on *time of signal start* calculation), $t_0 = 0\,\text{ns}$ was assigned to the signal. Events with no signal were easily excluded by this method.

ii) **second cut: t_0 before half sample times**: our second cut, applied on any of the channels except the Cherenkov one, excluded those events with t_0 bigger than 480 ns, which is half the time sampling duration for each signal on each event.

Since the BGO scintillation signal has a typical duration of several hundred ns, this cut made in such a way to limit including events in which the scintillation signal would be cut, before it would actually end, by the default time sampling duration.

This cut had a minimal effect, on average excluding a dozen events.

iii) **third cut: $t_0^{\mathrm{new}}(\mathbf{C})$ in a restricted interval**: the third cut ruled out the events *on the Cherenkov channel (C)* in which the jitter-corrected signal start time t_0^{new} lied outside the interval $[-30, -10]$ ns.

This cut significantly improved the precision on our measurement of Cherenkov light. A Cherenkov time of start that was consistent with the majority of the distribution (roughly within 3 std. dev. from the mean value, which was about -20 ns) was required. This ruled out a really sizeable amount (around 30%) of events that falsified the calculation of Cherenkov light yield.

As explained earlier, the Cherenkov jitter-corrected signal start times distribute around a mean value of roughly -20 ns, probably as a consequence of quicker response time of the PMT C with respect to the other PMTs.

In Figure 13 one can see the distribution of Cherenkov signal start times, upon which the choice for the interval around which to perform the cut can be understood.
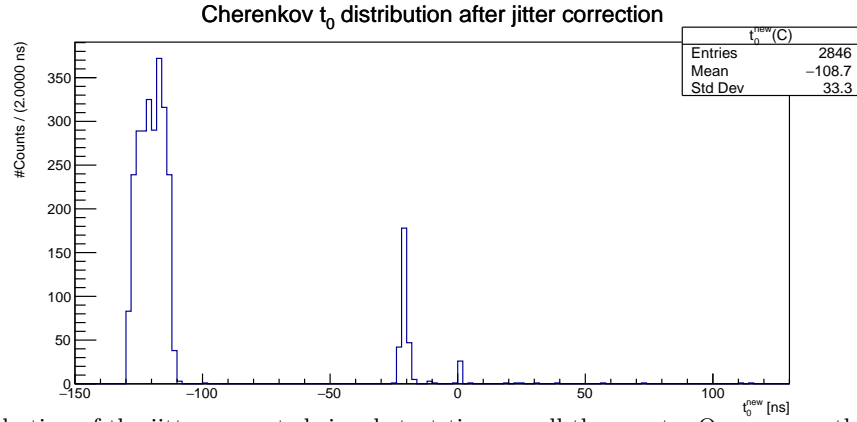

Figure 13 Distribution of the jitter-corrected signal start time on all the events. One can see the peak corresponding to "good events" centered around -20 ns.

iv) **fourth cut: $T_{\mathrm{mean}}(\mathbf{S})$ in a restricted interval**: a fourth cut was made to select all the events in which the scintillation mean time lied in the interval $(185, 320)$ ns.

This choice was made upon analyzing the histogram of the event-by-event distribution of mean times on the scintillation channel, which highlighted the presence of a small fraction of events (order of 2-3) that presented out-of-scale values as their mean times. We excluded those, then, as they do not represent physical scintillation events. Just for reference, Figure 14 shows the scintillation channel mean time distribution on a particular run before any cut is made (a). One notes a broad, background distribution against which a peak can be discerned in the $(200, 300)$ ns region. In (b) the charge distribution is shown, where one notes a number of events distributed around the value 3000 (the units are arbitrary), distinctly separated from an exponential background that concentrates around zero.
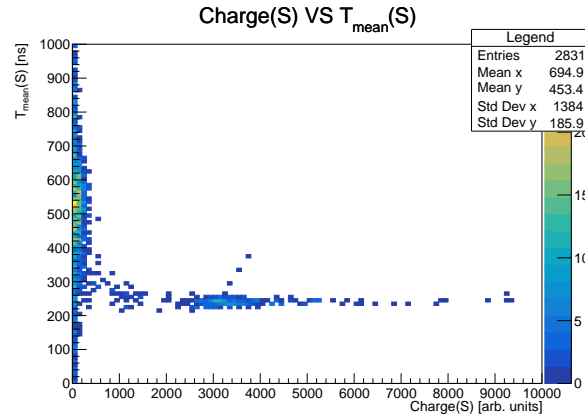
Figure 15 presents a two-dimensional charge vs T_{mean} distribution histogram, computed before performing the cuts aforementioned, alongside the two one-dimensional charge and mean time distribution histograms. One can easily spot a higher concentration of events in the $(2500, 4500) \times (200, 300)$ ns rectangle, which one could infer is the signal region. As one can see, a sizeable amount of events distributes outside of this region. The cuts we implemented were aimed at getting rid of a good fraction of those unphysical events.
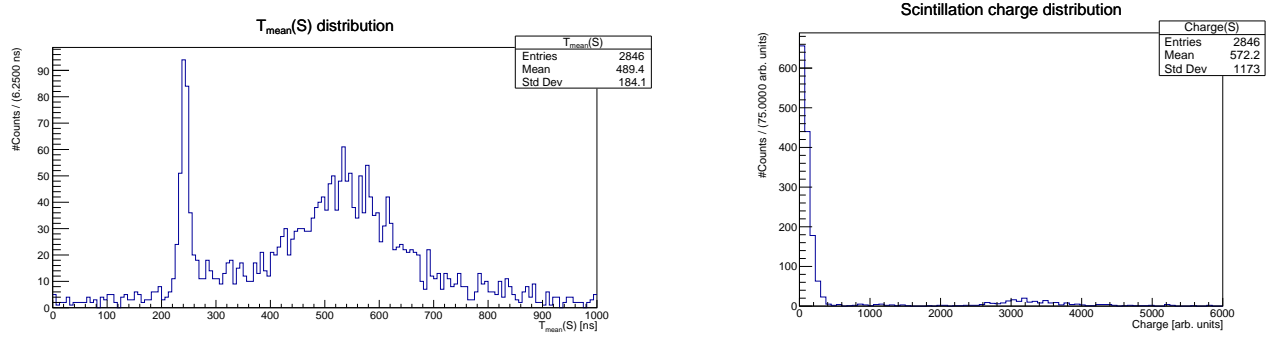
(a) Distribution of the mean time on the scintillation channel for all events. A broad noise distribution is present, along with a peaking number of events that distributes rather narrowly, corresponding to signal.

(b) Distribution of the charge on the scintillation channel for all events. The background distributes towards low charge values, while one can identify the signal events in the broad peak around 3000-3500 (arbitrary units).

Figure 14 Mean time and charge distributions on the scintillation channel, on all events.

Figure 15 Two-dimensional Charge vs T_{mean} distribution histogram.

   v) <u>**fifth cut: no signal saturation**</u>: the last cut that was implemented allows us to get rid of some saturated events. Saturation was checked on all channels, with a technique similar to the one pointed out in subsection 3.5. Order of 1-2 events per run showed saturation in the scintillation channel: we had to get rid of those because, even though they corresponded to physical events, they couldn't be used for calculation of the most basic quantities like the charge.

In Figure 16 one can see a "good event", i.e. an event that survived all the cut chain described above and that is, hence, a good candidate for signal. All the aforementioned features of the signals can be spot on the four channels. The P1 and P2 trigger channels (that naturally present a very consistent signal on all candidate events) have a very spiked and short scintillation signal. The scintillation channel shows a rather large impulse, with a really slow exponential dive, corresponding to a mean time in the hundreds ns region as expected. The Cherenkov signal is both less ample in height and in time duration, as expected. This makes in such a way that it is quite more easily mistakeable as background fluctuation, as mentioned before.
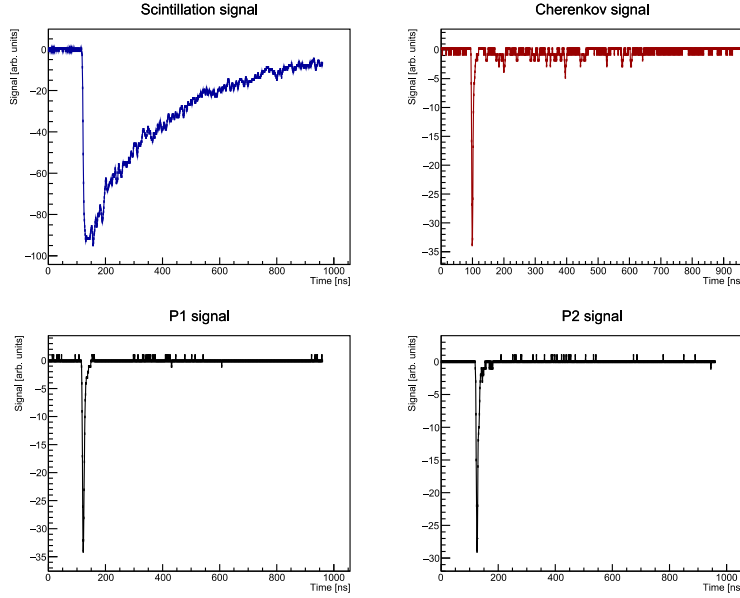
Figure 16 Example of a "good event". The scintillation channel (blue) has the most ample and longer-lasting signal, while one can see how the Cherenkov (red) and the P1 and P2 signals are way faster and smaller in amplitude.

Table 3 summarizes the cut chain flow for a specific $\theta = 29°$ run.

Table 3 $\theta = 29°$ run cut flow. One can see how the most demanding cuts are cut 1 (t_0 present, i.e. signal present in three channels) and cut 3 ($t_0^{\text{new}}(C)$ in restricted interval, i.e. Cherenkov signal start time in the most frequent region of its distribution).

Candidate events	After cut 1	After cut 2	After cut 3	After cut 4	After cut 5
2846	416	406	271	270	268

4.2 Signal analysis

The goal of our experiment is to measure the light yield ratio between Cherenkov and scintillation in the BGO crystal as a function of the inclination angle θ of the crystal. This should highlight a peak around $\theta = 28°$ (corresponding to $\varphi_C = 62°$, see subsection 1.1), which is the angle of Cherenkov light emission.

We are now going to describe the procedure used to determine the C/S ratio from the events that survive the cut chain explained earlier. In fact, this measurement can be done in several ways within our experimental setup. After introducing a main outline of the technique that we employed, we are going to differentiate between two methods and present their respective results.

As we mentioned earlier (see section 3), Cherenkov light is expected to have a much smaller yield than scintillation light. Additionally, despite we use a polarizing filter, we cannot eliminate completely the scintillation component from the Cherenkov channel. Consequently, the computation of the ratio goes as follows:

- for <u>Cherenkov</u>, one needs to subtract from C', the total light yield of the signal - which is proportional to the charge, the fraction S' of scintillation light that remains in the Cherenkov channel. S' is computed independently of the Cherenkov signal by rescaling the corresponding charge in the scintillation channel, $\tilde{S}$, by a factor r. C' and $\tilde{S}$ are calculated by integrating the signal on the interval $[t_0(\text{Ch}), t_0(\text{Ch}) + 20\,\text{ns}]$, with Ch = {C, S} and the 20 ns window chosen based on the rapidity of the Cherenkov signal;

- for <u>scintillation</u>, the procedure is way easier thanks to the fact that there is little to no contamination from Cherenkov. Then the light yield relative to scintillation only is assumed to be proportional to the charge in the scintillation channel, denoted as S, which corresponds to the integral of the scintillation signal on the interval $[t_0(S), t_{\text{sample}}]$[5].

As a result,

$$\frac{C}{S} := \frac{C' - S'}{S} = \frac{C' - r\,\tilde{S}}{S} \tag{8}$$

We took different approaches for calculating both the ratio between the quantities C and S, as defined above, and the rescaling parameter r. We tested two approaches for each task, and we are going to present here two combinations of those approaches.

First method for the C/S computation

As for the rescaling parameter r, we computed it *for each event* as the ratio between the areas under the signal curves of the Cherenkov and scintillation channels. In particular, since r should reproduce the fraction of scintillation light present in the Cherenkov signal, we calculated it as the ratio between the integral of the Cherenkov signal and the integral of the scintillation signal over the time interval $[t_0(\text{Ch}) + 20\,\text{ns}, t_{\text{sample}}]$, with $\text{Ch} = \{C, S\}$. In this region the signal on the Cherenkov channel should only show the long, remaining scintillation contamination.

For each angle, the C/S ratio was then calculated, using this method, as follows. Histograms in Figure 17a and Figure 17b show the distributions of events on which the quantities C and S were computed using Equation 8. Upon a first inspection, the distributions appeared Gaussians, possibly also thanks to sizeable statistics (about 150-300 "good" signal events on average). Hence, a Gaussian fit was applied to both the C and S distributions, from which the mean value and its error were extracted. Then the C/S ratio was indirectly computed as the ratio between these fitted C and S means, with the error propagating from the errors on the mean values.
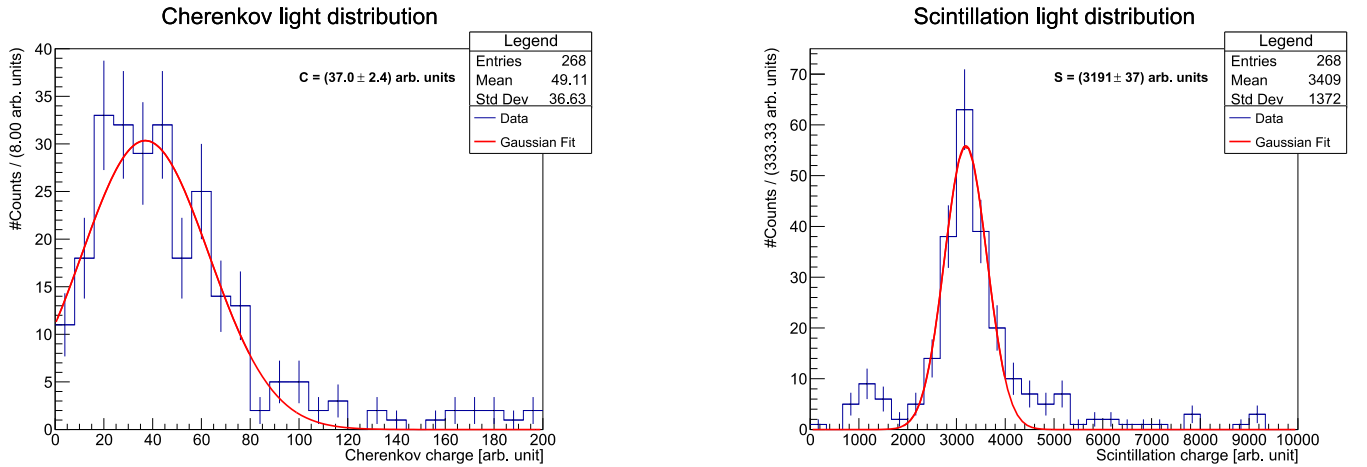
(a) Histogram of event-by-event Cherenkov charge distribution at $\theta = 29°$. The fitted Gaussian is shown in solid red. The result of the fit for the Cherenkov charge is $C = (37.0 \pm 2.4)$ arb. units.

(b) Histogram of event-by-event scintillation charge distribution at $\theta = 29°$. The fitted Gaussian is shown in solid red. The result of the fit for the scintillation charge is $S = (3191 \pm 37)$ arb. units.

Figure 17 Distributions of event-by-event Cherenkov and scintillation charge in the context of "method 1". The Gaussian fits are also shown.

---

[5]We remind that $t_{\text{sample}} = 960\,\text{ns}$ is the maximum sampling time for each signal.
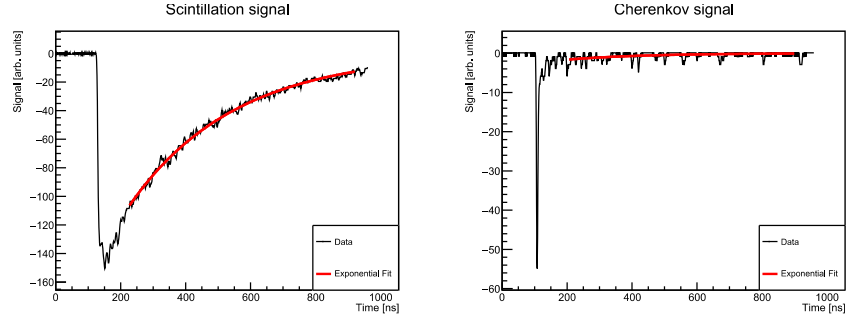
Second method for the C/S computation

A second method saw the calculation of r made in a different way. r is computed as the ratio between the amplitudes, rather than the charge, of the scintillation measured in the Cherenkov and the scintillation channels - a quantity still proportional to the energy release. This procedure was carried out by fitting *for each event* the signals on the scintillation and on the Cherenkov channels, over the time interval $[t_0(\text{Ch}) + 100\,\text{ns}, t_0(\text{Ch}) + 800\,\text{ns}]$. Here r was defined as the ratio between the amplitude fitted from Cherenkov signal and the one fitted from scintillation. The fits were made to exponential functions

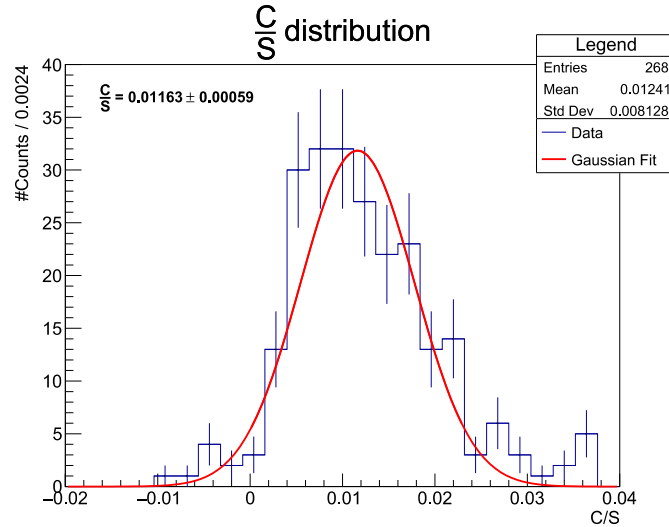$$S_{\text{fit}} = A\,e^{-t/\tau} \quad C_{\text{fit}} = B\,e^{-t/\tau} \quad , \tag{9}$$

so that $r = \frac{B}{A}$. τ is the average scintillation time, and it was estimated from the fit on the scintillation signal, while it was given as input for performing the fit to the Cherenkov signal. Figure 18 shows an example of event on the scintillation and Cherenkov channel for a particular run. The black line is the signal, while the red line is the fitted exponential.

The ratio C/S was calculated, *for each event*, as shown in Equation 8. In order to get an estimate, for the particular

Figure 18 Signal exponential fits on the scintillation and Cherenkov channels, for a particular event (probably a good event) on the 29° run. These were employed in the context of "method 2", in order to compute the ratio r as the ratio between the two fitted exponential amplitudes.

run, of the C/S ratio at the corresponding angle θ, we examined the histogram of the C/S ratio values computed *for all events*. Upon noticing, once again, that the distribution generally looked like it satisfied the Gaussian approximation, we fitted to Gaussian the distribution of the C/S values (see Figure 19) and extracted a result as the mean value with its error associated.

Figure 19 Histogram of the distribution of the C/S values computed for the signal candidate events for $\theta = 29°$. The Gaussian approximation looks satisfied, hence the value $\frac{C}{S} = 0.0116 \pm 0.0006$ was obtained through a Gaussian fit shown in solid red.

The choice of those two methods has essentially come down to a very simple aspect. Among the four possible combinations of the two methods of calculating r and C/S (that are independent one from the other), we selected those that preserved as much as possible the Gaussian approximation for the distributions we wanted to fit. We observed that this choice had an impact on the final measurement, that we will cover more in detail in subsection 4.3. The two methods we picked were also the ones that in the end reflected better the expected behavior of the C/S ratio as a function of the angle θ.

Error estimation

As it has briefly been mentioned in the previous paragraphs, the estimation of the errors on our measurement of C/S was almost purely statistical. The reason for this is that the systematical effects could not be estimated precisely, and in particular they could only be under-estimated, resulting in little to no contribution to the final error estimation. The only systematic effect we could calculate would be a 1-channel/$\sqrt{12}$, digital error on the TD signal values for each sample time, which constituted a rather great under-estimation.

That is why we adopted, in both methods, the errors on the mean values from the Gaussian fits to the histograms, propagating, in the case of the first method, the errors from the fits to C and S distributions.

4.3 Results

In this final section of our analysis, we present the results of the C/S ratio measurements at various tilt angles of the BGO. Data were collected at thirteen different positions of the BGO, corresponding to the angles θ listed in Table 4. The table shows, along with the angle configurations, also the relative error, which is estimated as a systematic uncertainty of 0.1° due to the measurement technique employed, using the smartphone app `Phyphox`. Additionally, the table provides also the total number of events (i.e. the events selected by the trigger) and the number of events after the cuts. It is to be remarked that the same choice of cuts (covered in subsection 4.1) has been implemented on all measurements at various angles.

Table 4 Experimental values of the angles at which the measurement of the C/S ratio was done (with error). Also in the table, the number of events before and after the sequence of cuts are shown.

| θ [deg]	-31.2	0.5	10.5	20.3	22.5	25.6	28.4	29.3	30.8	32.3	34.8	39.7	45.1
σ_θ [deg]							0.1						
Total events	2122	2331	3129	2536	1509	2438	1920	2846	2661	2466	2778	3010	2429
Events after cuts	106	143	293	251	151	240	167	268	271	234	240	255	239

C/S ratio

Figure 20 displays the results relative to the C/S measurements. The blue points are the experimental points relative to the first method, while the red ones were obtained through the second method. We observe that:

- With both methods there is a maximum in the C/S ratio, as expected;

- In both cases, the behavior of the C/S ratio around this maximum is consistent with predictions based on geometrical considerations for the emission and propagation of Cherenkov and scintillation light in our detector (see subsection 1.4);

- Our measurements of the C/S ratio suggest a maximum value around 32 ° (first method) and 29 ° (second method). This analysis does not have the means to precisely determine the C/S peak, as in order to do

so one would need to fit the data to a theoretical distribution, which unfortunately we don't have at our disposal. As for the angles, for example, the 0.1° uncertainty on the angles is surely an under-estimation. To try to explain why, one could consider that the table on which the experimental apparatus was built, and stayed for the whole duration of the experiment, was not perfectly fixed into place, and hence could suffer minimal movements. Furthermore, gravity made in such a way that the wooden tray that contained the BGO could be seen changing its position towards sligthly ($\sim 0.05°$) greater angles over an acquisition run;

- As a purely technical remark, we were able to take more measurements to the left of the peak than to the right, because of the limited geometrical freedom of our setup;

- Based on the results for the peaks and the theoretical expectation of a peak at 28°, the second method appears to be the most preferable, as it yielded a more accurate result with respect to the predicted value;

- With this in mind, though, also considering the uncertainty on our angle measurements, we feel like we should not interpret the first method result as unsuccessful. Our measurement of the C/S ratio does not have the prerogative of calculating a peak with extremely high precision, but rather to validate the expected behavior around a peak approximately in the region of the predicted 28°, which both methods accomplish in a satisfactory way.
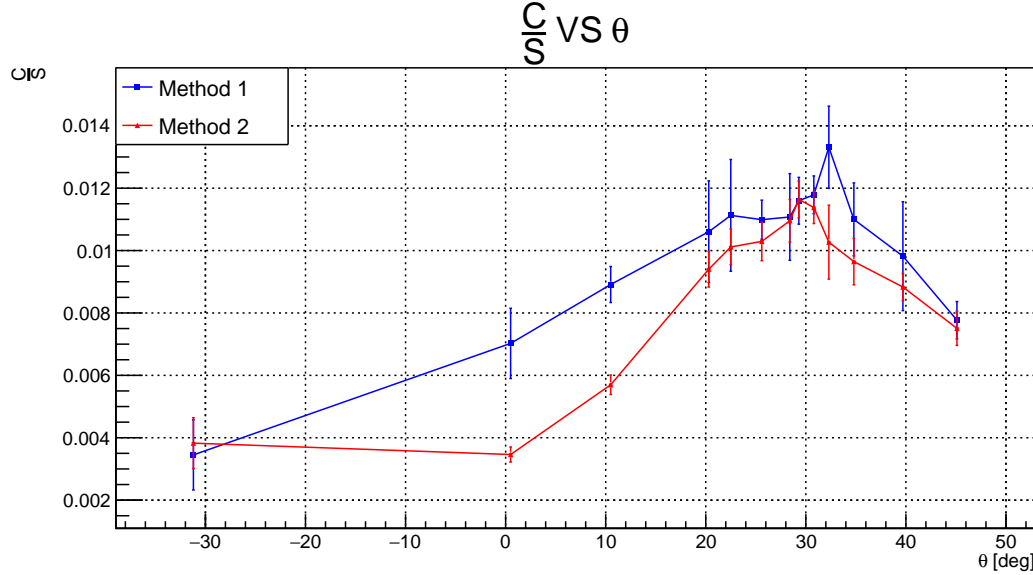
Figure 20 The plot shows the results of the measurement of the C/S ratio with the two methods we employed. The blue points correspond to the first method, while the red points to the second. One can observe a general agreement of the behaviors of the C/S ratio between the two methods.

In light of these considerations, we believe our measurement fulfills our initial purpose of verifying the C/S behavior as a function of the BGO angle. The final step in this validation will come from simulation, which will be covered in section 5.

Based on our experience, we would suggest future experimentalists willing to reproduce this measurement to use the second method presented in our analysis.

Scintillation analysis

We present here also some brief considerations on the study of scintillation light emission in our experiment, in the form of a *light yield versus angle* analysis and a *scintillation average time* analysis.

As for the scintillation yield, we expect a $\propto \frac{1}{\cos \theta}$ behavior (as subsection 1.4 reminds). This study then offers the opportunity to validate this. Figure 21 shows a plot of the scintillation light yield versus θ. The scintillation light yield, as mentioned in the previous sections, is the integral of the scintillation channel signal. We generally denote a very good accordance between the experimental points and the predicted behavior, with almost all of the points within one or two sigmas of the yellow dashed line (with the only exception of the $\theta = -31.2°$ point). We limit ourselves to observe accordance in a rather qualitative way without performing any fit to the data, as this would be outside the purpose of our analysis.
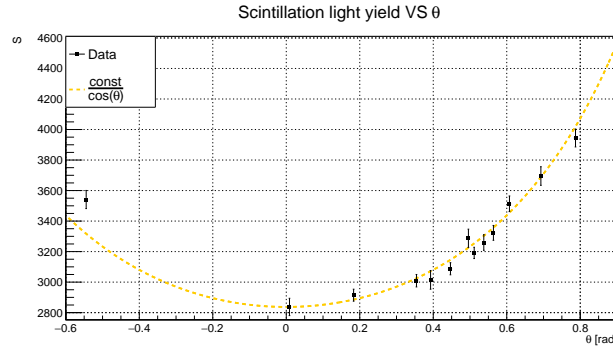

Figure 21 Experimental (black points) and theoretical behavior (yellow dashed line) of the scintillation light yield versus angle. As expected the data follows $\propto \frac{1}{\cos \theta}$.

Figure 22 is relative to the scintillation time analysis. In Figure 22a is an example of event-by-event distribution of scintillation times, obtained in the context of method two (subsection 4.2). For every angle we fitted the histogram of scintillation average times to Gaussian in order to extract the value of τ that was then used to fit the Cherenkov component.

The scintillation times obtained for all data runs are plotted versus angle in Figure 22b (black points). The mean value, along with its standard deviation, is also shown. We observe that most of the points lie within one standard deviation of the mean value. One also observes that the mean value is slighlty off-set from the expected scintillation time of the BGO. This is because there are other scintillating components in the crystal that are suppressed with respect to the main, 300 ns, component, that have a scintillation time around 60 ns and contribute to slightly lowering the scintillation time of the crystal.
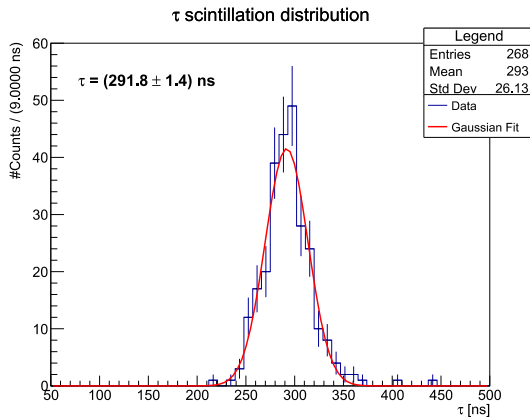
(a) Distribution of scintillation τ for $\theta = 29$ °. Also shown is the Gaussian fit to the histogram, which yields an average $\tau = (291.8 \pm 1.4)$ ns.
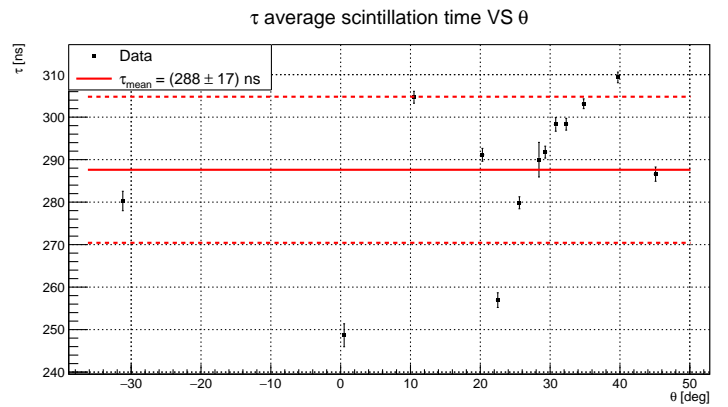
(b) τ versus angle. One observes how the experimental points most of the times lie within one sigma of the mean value, suggesting a general consistency of the measurement. The mean value (288 ± 17) ns is slightly lower than the expected 300 ns because of fast-scintillating components in the BGO.

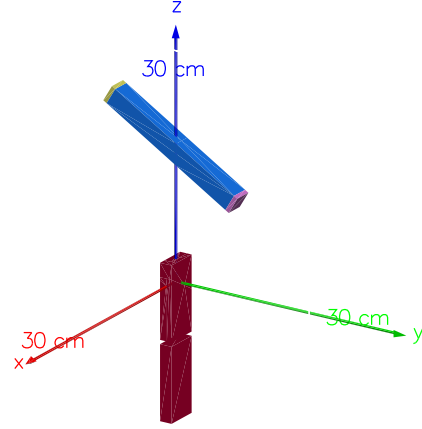**Figure 22** Plots relative to the scintillation time analysis.

24

5   Geant4 simulation

In order to validate the experimental results and compare them with theoretical predictions, a simulation was conducted using `Geant4`. This study is divided into two main parts: first, we calibrated the plastic scintillators and compared the event rates with the experimental ones, then we measured the C/S ratio at different angles by counting the number of photons reaching the two PMTs.

5.1   Detector geometry

The simulated apparatus has a simpler geometry compared to the experimental setup. In particular, the wooden structure supporting the various components and the box containing the crystal and the photomultipliers connected to it are omitted.

The size and the component of each material were defined using `G4Box` and `G4Material`, respectively. These components were then assembled using `G4LogicalVolume`, and finally placed in specific positions in the space using `G4VPhysicalVolume`. This space, referred to as the World, is filled with air and serves as the environment where particles are generated. The BGO crystal is placed at the top of the World, with both ends connected to two boxes that represent photomultiplier tubes. These are both made of Pyrex glass, but serve dif-

Figure 23 Picture of the simulated apparatus. The blue parallelepiped represents the BGO crystal, which is connected at both ends to the PMTs. The yellow box on the top of it is the PMT designed to detect scintillation light, while the purple one on the bottom is for Cherenkov light. The two red boxes at the bottom represent the plastic scintillators.

ferent purposes: one photomultiplier tube is employed to detect Cherenkov light (PMT C), while the other detects scintillation photons (PMT S). The BGO crystal, along with the PMTs, can rotate around the z axis, forming an angle θ with it. This feature allows the simulation to replicate the conditions and measurements carried out in the laboratory. Below this structure are placed the two plastic scintillators (P1 and P2).

All volumes are treated as scoring volumes, which means that they can record the amount of energy deposited (in the BGO crystal and the plastic scintillators) and the number of photons produced (in the case of the PMTs). Figure 23 shows the detector geometry, while Table 5 summarizes the properties of each component of the apparatus. The dimensions are obtained by halving those of the actual experiment.

Table 5 Dimensions ($x \times y \times z$), material, and density of each system element.

Name	Dimensions [cm]	Material	Density [g/cm^3]
World	$50 \times 50 \times 50$	G4_AIR	0.0012
BGO crystal	$1.1 \times 9 \times 1.1$	G4_BGO	7.13
PMT C and PMT S	$1.1 \times 0.25 \times 1.1$	G4_Pyrex_Glass	2.23
P1 and P2	$2.75 \times 0.5 \times 4.75$	G4_PLASTIC_SC_VINYLTOLUENE	1.032

Finally, to recreate the polarizing filter used to distinguish Cherenkov photons reaching the PMTs, we applied a condition on the counting of photons in each PMT, requiring that PMT C only detects Cherenkov photons, while the PMT S is devoted only to scintillation photons.

5.2 Generation of muons

Cosmic muons with a fixed energy of $4\,\mathrm{GeV}$ were generated using the tangent plane method. Specifically, a sphere with a radius of $R = 30\,\mathrm{cm}$, centered on the geometric center of the apparatus, was used. This sphere is small enough to achieve high efficiency while being large enough to contain the entire system.

A point (ϕ, θ) was placed on the sphere: the angle ϕ is drawn uniformly in $[0, 2\pi]$, while θ is selected between 0 and $\pi/2$ according to the muon angular distribution, assumed to be proportional to $cos^2(\theta)$. A tangent plane of size $2R \times 2R$ was constructed on this point. To generate muons, we start from the point $P(x, y, z = R)$, with both x and y in the range $[-R, R]$. The coordinates are then transformed into the coordinate system S', which is obtained by rotating the initial system of an angle θ around y axis:

$$\begin{pmatrix} x' \\ y' \\ z' \end{pmatrix} = \begin{pmatrix} \cos\theta & 0 & \sin\theta \\ 0 & 1 & 0 \\ -\sin\theta & 0 & \cos\theta \end{pmatrix} \begin{pmatrix} x \\ y \\ z \end{pmatrix} \tag{10}$$

The system then rotates by an angle ϕ around the z' axis, resulting in

$$\begin{pmatrix} x'' \\ y'' \\ z'' \end{pmatrix} = \begin{pmatrix} \cos\phi\cos\theta & -\sin\phi & \cos\phi\sin\theta \\ \sin\phi\cos\theta & \cos\phi & \sin\phi\sin\theta \\ -\sin\theta & 0 & \cos\theta \end{pmatrix} \begin{pmatrix} x \\ y \\ z \end{pmatrix} \tag{11}$$

The generated point is finally translated along the positive z axis by $5\,\mathrm{cm}$ to ensure the particles reach the detector components.

Using the physics lists `G4EmStandardPhysics` and `G4OpticalPhysics`, it is possible to generate not only the primary muons but also the secondary particles produced from their interaction with the material, specifically the photons, which are the focus of the second part of the analysis.

5.3 Calibration of the system

The first part of the simulation focuses on calibrating the system energy measurements to compare the experimental energy spectra with those obtained from `Geant4`. Ten million muons were simulated within the sphere, where the BGO crystal was inclined at an angle θ^{*}[6]. In particular, to record the event the particle had to cross both plastic scintillators, ensuring an energy deposit in each scintillator greater than $0\,\mathrm{MeV}$ (double coincidence). The duration of the experimental data acquisition corresponds to a laboratory measurement time calculated as

$$T_{sim} = \frac{N_\mu}{\phi_\mu\,[\mathrm{cm^{-2}\,s^{-1}}] \cdot A\,[\mathrm{cm^2}]} = \frac{10^7}{0.019\,\mathrm{cm^{-2}\,s^{-1}} \cdot (60 \cdot 60)\,\mathrm{cm^2}} = 146198\,\mathrm{s} \approx 40.6\,\mathrm{h} \tag{12}$$

where N_μ is the number of simulated muons, ϕ_μ is the muon flux, and A is the area of the tangent plane on the sphere. The time value allows to normalize the histograms of counts, so to obtain the rate histograms as a function of the released energy.

At this stage, we focused on calibrating the BGO crystal and the trigger system, operating in double coincidence mode.

---

[6]This angle is $\theta^* = 30.8°$, and it has been introduced in subsection 3.3.

5.3.1 Calibration of plastic scintillators

As seen for the Cherenkov and the scintillation light charge distribution, the energy spectra deposited in the plastic scintillators P1 and P2 exhibit a dual behavior. At low energies, a long exponential tail emerges, caused by muons not crossing the system vertically. At higher energies, a small peak appears, which can be fitted with a Gaussian distribution and is attributed to vertically traversing muons. To determine the calibration factor, Gaussian fits were performed on the histograms for both scintillators using data from both simulations (sim) and experiments (lab). Figure 24 shows the energy deposited by muons in each plastic scintillator for θ^*.
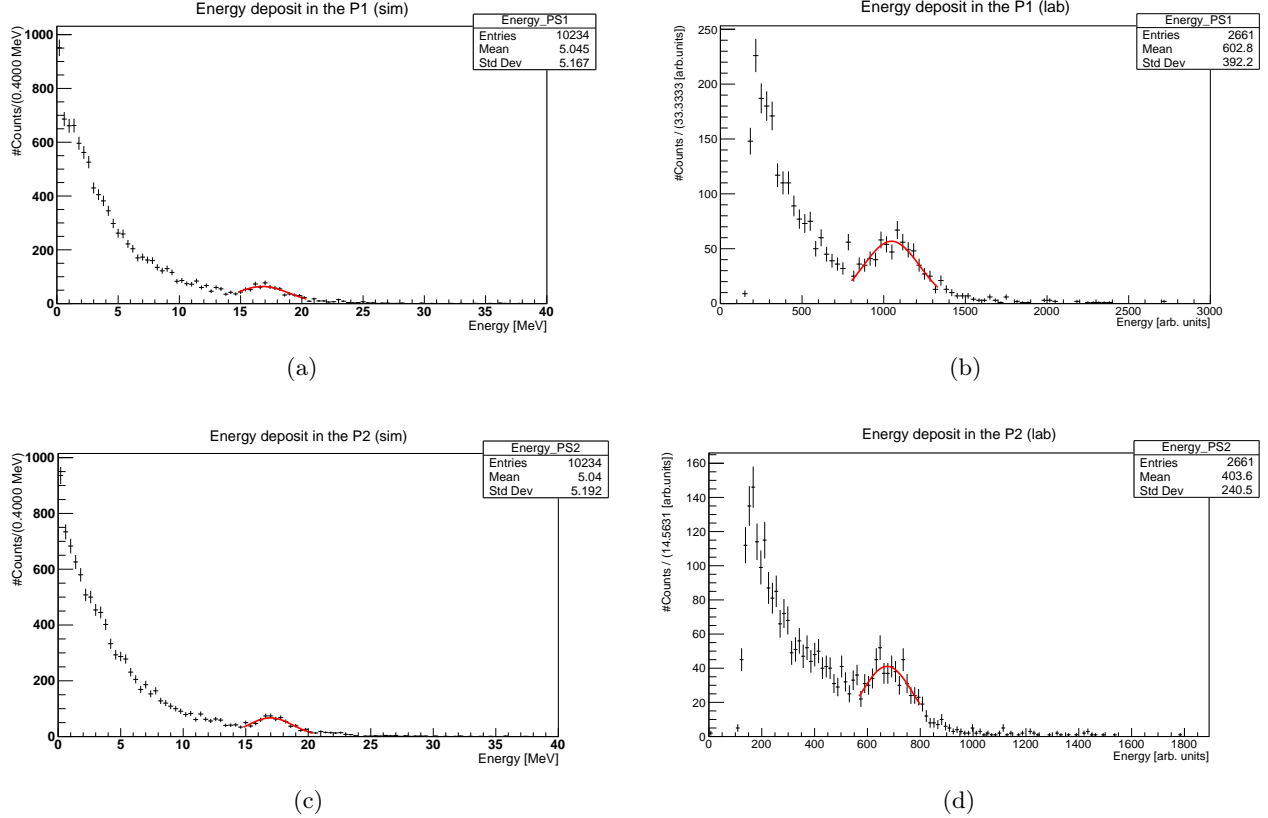
Figure 24 Histograms of the simulated and experimental energy spectra for the plastic scintillators at θ^*, with the solid red lines indicating the Gaussian fit. The top row displays the plots for P1: (a) shows the simulated spectra and (b) the experimental one. The bottom row shows the corresponding plots for P2: (c) presents the simulated spectra and (d) the experimental data.

The mean values obtained from the Gaussian fits on the peaks are the following:

$$\begin{aligned} \mathrm{E}_{P1}^{\mathrm{sim}} &= (16.80 \pm 0.17)\,\mathrm{MeV} & E_{P1}^{\mathrm{lab}} &= (1055 \pm 10)\,\mathrm{arb.\ units} \\ E_{P2}^{\mathrm{sim}} &= (17.06 \pm 0.11)\,\mathrm{MeV} & E_{P2}^{\mathrm{lab}} &= (670.2 \pm 7.8)\,\mathrm{arb.\ units} \end{aligned} \tag{13}$$

The calibration factor $\mathcal{F}$ is obtained by dividing the mean value of the experimental spectrum by that of the simulated energy spectrum. The associated uncertainty is calculated using error propagation methods.

$$\mathcal{F}_{P1} = 62.80 \pm 0.87 \qquad\qquad \mathcal{F}_{P2} = 39.28 \pm 0.52 \tag{14}$$

The calibration factor for the first plastic scintillator is higher than the one for the second plastic because of its larger amplification constant, as explained in subsection 3.1.

The simulated and experimental rates can now be compared. To plot the rate as a function of energy, the simulated counts are divided by the simulation time T_{sim}, while the experimental counts are divided by $T_{lab} = 259200\,s$, corresponding to the duration of each acquisition run (3 days). Additionally, the spectrum obtained in the laboratory is divided by the calibration factor.

In order to have a fair comparison between experiment and simulation, we also had to discard the events with too low energy in the simulation: after some try at lower energies, where we still had differences between the two histograms, we found out that the best choice, in order to maximize the overlapping, was to make a cut at 4 MeV. The rate histograms for both scintillators for θ^* are presented in Figure 25.
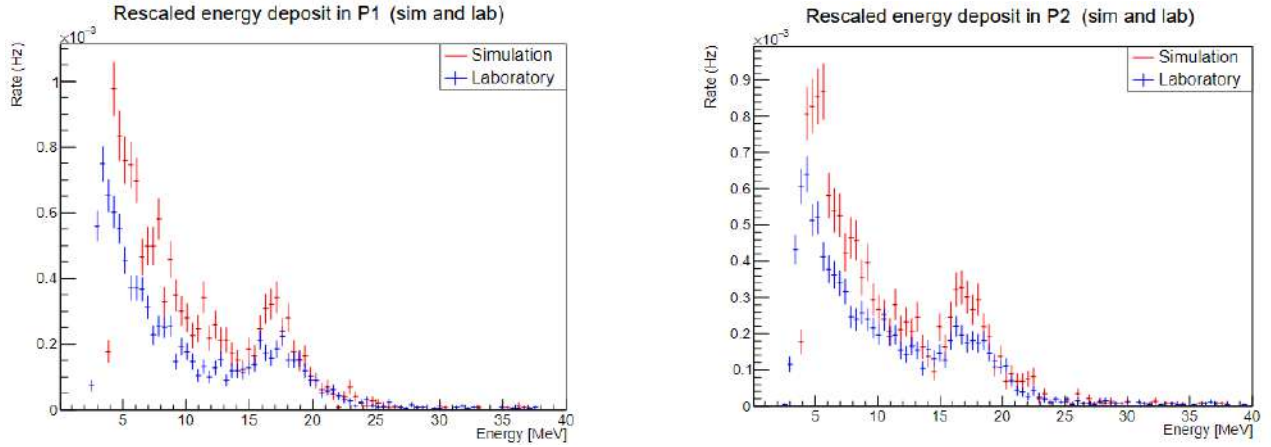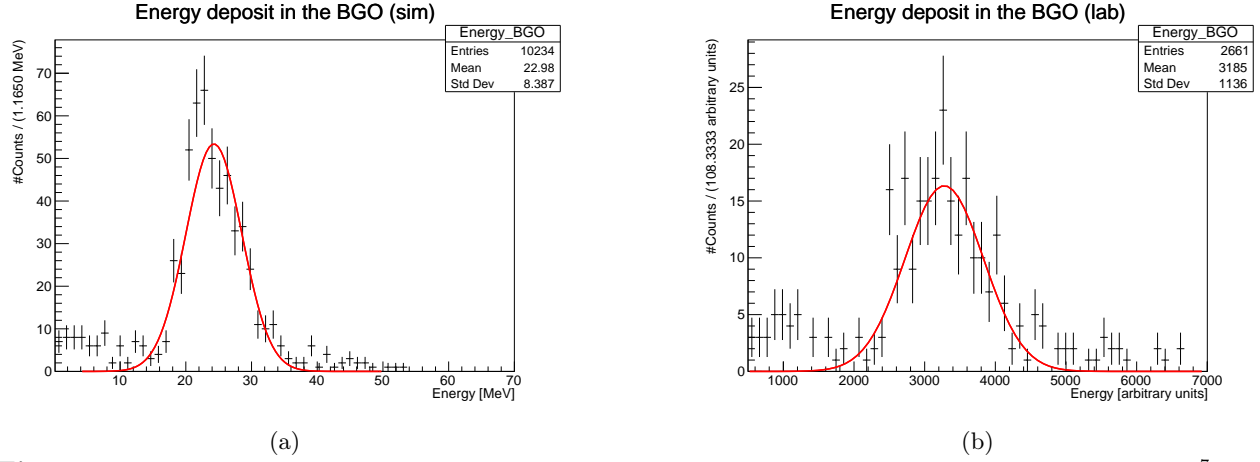

Figure 25 Scaled histograms of the rate: in red, the simulation results; in blue, the experimental results.

5.3.2   Calibration of the BGO crystal

It is also necessary to calibrate the measurements of the energy released in the BGO. To achieve this, a comparison is made with the experimental data recorded by the PMT used to detect scintillation photons, due to the fact that the number of photons is proportional to the deposited energy. For the chosen angle, θ^*, the energy deposited via scintillation is correlated with the total energy deposited in the BGO. In this case, it is therefore possible to compare the experimental histogram of scintillation energy with the simulated histogram for the BGO, which captures all the energy of the incoming muons.

In both cases there's a peak that can be fitted using Gaussian distribution, as can be seen in Figure 26.

(a)

(b)

Figure 26 Histograms of deposited energy at θ^*: 26a is the simulated histogram, 26b is the experimental one[7]. In both cases, the graphs focus on the area where the peak is present.

The mean values resulting from the fit are

$$E_{BGO}^{sim} = (23.84 \pm 0.26)\,\text{MeV} \qquad\qquad E_{scint}^{lab} = (3207.58 \pm 59.94)\,\text{arb. units} \qquad (15)$$

thus the calibration factor is equal to $\mathcal{F} = 134.5 \pm 2.9$. The re-scaled histograms, obtained as described in subsubsection 5.3.1, are shown in Figure 27.
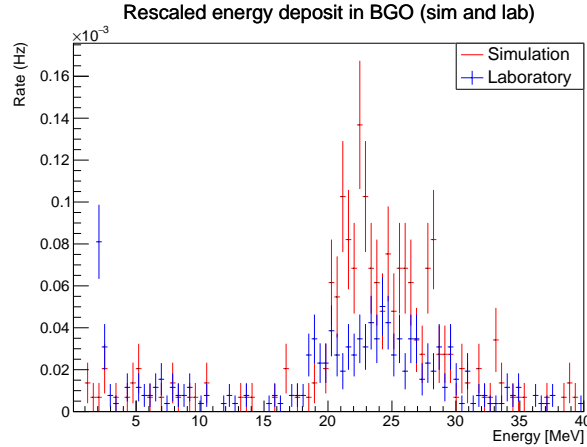
Figure 27 Scaled histograms of the rate: in red, the simulation results; in blue, the experimental results.

An analysis on the distribution of peaks for all measured angles was also performed. It is expected that the points follow a behavior proportional to $\frac{1}{\cos\theta}$, as previously shown in Figure 4.3.
Figure 28 shows the obtained behavior, which was fitted with the function $y = a/\cos\theta$, where θ is the angle of inclination of the crystal.

---

[7]Note that we're referring to the energy deposit in the BGO, but as explained before this energy is equal to the scintillation energy.

Fit on the maximum energy deposit in the BGO crystal as a function of the angle
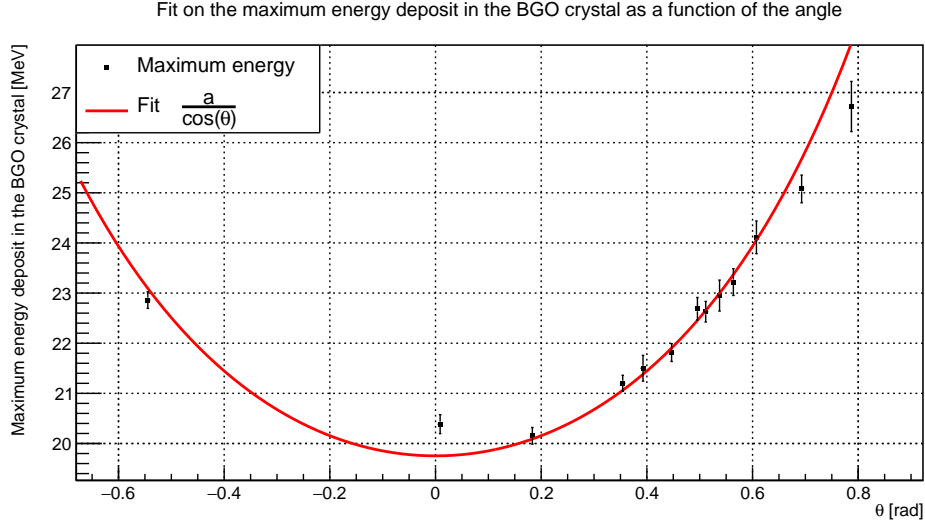
Figure 28 Distribution of the maximum energy deposit values in the BGO crystal as a function of the angle of inclination θ [rad]. The red line represents the fit performed on the distribution.

The parameter a was treated as a free parameter, with the resulting value $a = (19.753 \pm 0.054)$ MeV. We can underline a good accordance between the experimental points and the fitting curve within 2σ, confirming what we got in the experimental analysis.

5.4   Measurement of C/S ratio

It is now possible to simulate the photon production and calculate the C/S ratio. Unlike the laboratory setup, we did not recreate the polarizing filter. We remind that such filter reduces both contributions from Cherenkov and scintillation, but it greatly improves our resolution on the Cherenkov part since the scintillation part is reduced more than the Cherenkov part. As said in subsection 5.1, instead of the filter we required that PMT C only detects photons coming from Cherenkov effect and PMT S those from scintillation.

5.4.1   Detector properties

In order to study the ratio between Cherenkov and scintillation photons produced by muons crossing the system and interacting with the materials, it was necessary to take into account optical properties of the apparatus in the simulation. In `Geant4` it is possible to define a set of value for each observables with their corresponding energies, then the program performs an interpolation between these values. To accurately model interactions at the boundaries between different materials and components, we defined the optical surfaces, in particular for the pairs BGO-PMT, BGO-air, and PMT-air. These affect how light, i.e. photons, is reflected and refracted at these boundaries.
Specifically we set the following properties across various energies within the visibile spectrum (for the references see [4], [5] and [6]):

- World: refractive index;

- BGO crystal: refractive index, relative intensity of scintillation light, absorption length, scintillation time constant $\tau = 300$ ns, scintillation light yield $LY = 8000 \, \gamma/\text{MeV}$, resolution scale equal to 1, reflectivy and transmittance;

- PMT C and PMT S: refractive index, resolution scale equal to 1, relative intensity of scintillation light, which is constant over the energy range of interest.

5.4.2   Vertical muons

In order to make sure that our choice of the optical properties described properly the system, we firstly simulated 1000 vertically crossing muons for each angle at which the BGO crystal was tilted in the laboratory. Since the muons were vertical, all of them were suitable for the subsequent analysis.

The C/S plot was obtained by dividing the mean value of the Cherenkov photons distribution by the one of scintillation photons, both found applying a Gaussian fit on the peaks in the photon spectra. The result is shown in Figure 29.
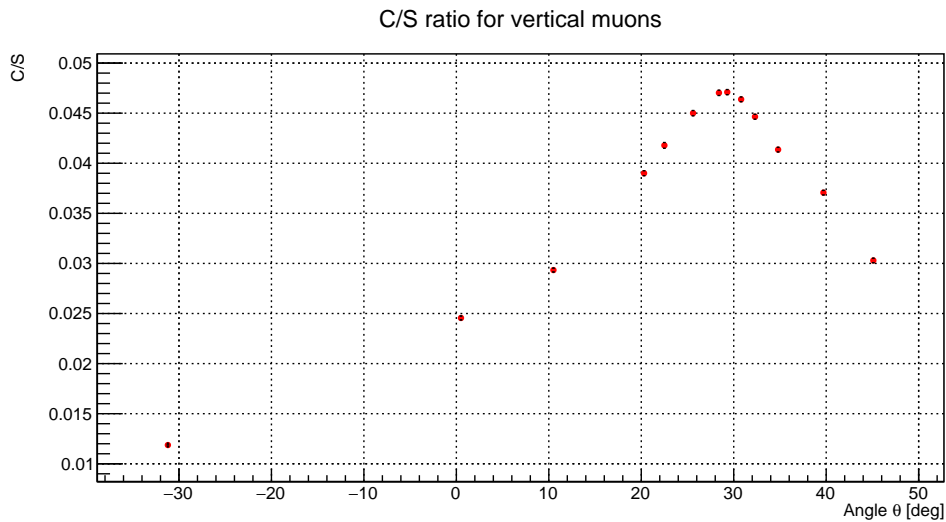
Figure 29 Distribution of the C/S ratio as a function of the angle θ for vertical muons. The uncertainties are of the order of 10^{-4}.

The simulation results align with the expectations, confirming the presence of a peak in the C/S ratio between the angles $28.4°$ and $29.3°$, as observed in the graph. Moreover, as the angle increases beyond the peak the C/S ratio decreases, indicating that the Cherenkov light contribution diminishes relative to scintillation light. This behavior confirms the dependence of the Cherenkov light on the angle, as was explained in subsection 1.1

5.4.3   Sphere method

We now simulate 5 million muons generated in the sphere which fully contains the system. As in the simulation of vertical muons, the angles are those chosen in the laboratory. In this case we required that to record the events the energy deposit in the two plastic scintillators, that we remind work as trigger system, must be larger than 4 MeV. This is the same value that was chosen in subsubsection 5.3.1 in order to select, in the simulation, the most suitable events with the experiment. In order to have more precise histograms of the Cherenkov light we cut the events below 50 photons while for the scintillation light we made the cut at 1000.

As done in the previous case, we fitted with a Gaussian the peak in both spectra and evaluated the C/S ratio as the ratio between the mean values of the photon counts. The behavior can be seen in Figure 30.
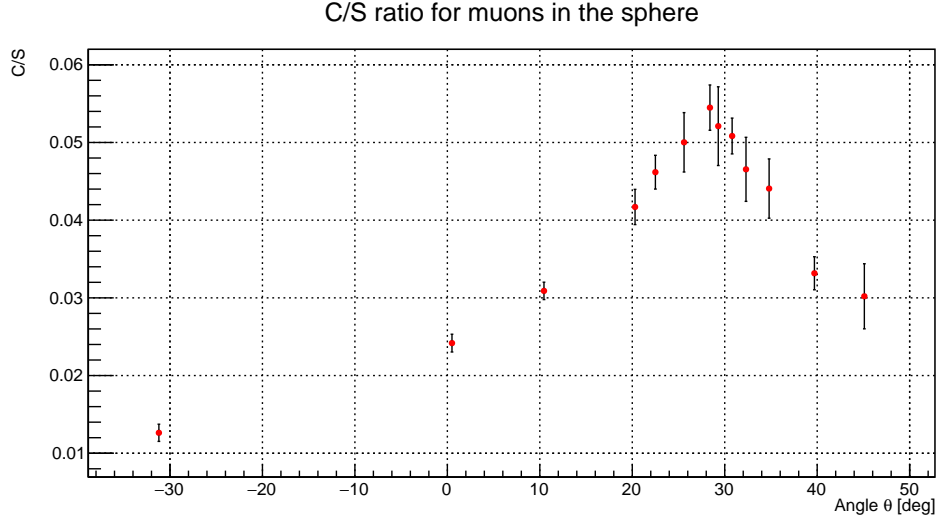
Figure 30 Distribution of the C/S ratio as a function of the angle θ for muons generated using the sphere method.

Also in this case the behavior is aligned with the expectations and with the experimental results from laboratory. A peak around 28° is well visible, confirming the maximum Cherenkov emission predicted by the theory.

6   Conclusions

Our experiment has put its focus on the calibration and testing of a BGO detector, with the aim of studying the ratio between Cherenkov light and scintillation light. This quantity has an angle dependence, which we investigated by tilting the BGO crystal on a horizontal axis.

Our analysis has found a peak, as visible in Figure 20, at $(32.3\pm0.1)°$ with a first method and $(29.3\pm0.1)°$ with a second method. This behavior is consistent with a theoretical expectance of a maximum in the Cherenkov light yield around 28°. We validated our analysis through a `Geant4` simulation, which showed a peak in the C/S ratio in two configurations, between 28.4° and 29.3° with a first method simulating 1000 vertically-crossing muons, and at 28.4° with a second method 5 million muons generated within a sphere.

References

[1] J.L. Autran et al. "Characterization of atmospheric muons at sea level using a cosmic ray telescope". In: *Nuclear Instruments and Methods in Physics Research Section A: Accelerators, Spectrometers, Detectors and Associated Equipment* 903 (2018). DOI: `10.1016/j.nima.2018.06.038`.

[2] Hadiseh Alaeian. *An Introduction to Cherenkov Radiation*. Mar. 2014. URL: `http://large.stanford.edu/courses/2014/ph241/alaeian2/`.

[3] *The Straggling Function. Energy Loss Distribution of Charged Particles in Silicon Layers*. URL: `https://www.scienceshot.com/post/the-straggling-function-energy-loss-distribution-of-charged-particles-in-silicon-layers`.

[4] M. N. Polyanskiy. "Refractiveindex.info database of optical constants". In: *Scientific Data* 11.94 (2024). DOI: `10.1038/s41597-023-02898-2`.

[5] G. Jellison et al. "Optical properties of bismuth germanate". In: *Journal of Applied Physics* 107 (Feb. 2010), pp. 013514–013514. DOI: `10.1063/1.3272909`.

[6] *BGO - Bismuth Germanate Scintillation material*. Saint-Gobain Crystals. URL: `https://www.luxiumsolutions.com/sites/default/files/2021-09/BGO-material-data-sheet.pdf`.

[7] M. Livan and R. Wigmans. *Calorimetry for Collider Physics, an Introduction*. Springer Cham, 2019. DOI: `10.1007/978-3-030-23653-3`.

[8] Electronics crate datasheets. URL: `https://www.caen.it/download/`.

[9] Example B1. Geant4 Collaboration. URL: `https://gitlab.cern.ch/geant4/geant4/-/tree/master/examples/basic/B1?ref_type=heads`.

[10] *Book For Application Developers*. Geant4 Collaboration. 2023. URL: `https://geant4-userdoc.web.cern.ch/UsersGuides/ForApplicationDeveloper/html/index.html`.